# ANALYSIS OF HYDROXYLAMMONIUM NITRATE BURNING RATES

A Thesis

by

JACOB MAC STAHL

Submitted to the Office of Graduate and Professional Studies of
Texas A&M University
in partial fulfillment of the requirements for the degree of

MASTER OF SCIENCE

| | |
|---|---|
| Chair of Committee, | Eric Petersen |
| Committee Members, | Sungyon Lee |
| | Adonios Karpetis |
| Head of Department, | Andreas Polycarpou |

May 2017

Major Subject: Mechanical Engineering

# ABSTRACT

Recent interest in the replacement of hydrazine as a liquid monopropellant has focused on the use of hydroxylammonium nitrate (HAN)-based monopropellants. HAN-based monopropellants offer benefits of improved performance and safer handling when compared to hydrazine, though its combustion properties are not as well understood as hydrazine. The work presented in this thesis seeks to improve the understanding of the combustion properties of HAN by conducting fundamental experiments to measure the burning rate of 82.4 weight percent aqueous HAN solutions. To verify the accuracy of these burning rate measurements, two methods were used to simultaneously measure the burning rate of aqueous HAN inside of a constant-volume pressurized strand burner for test pressures ranging from 2.37 to 15.10 MPa. This required the development of a method to measure the burning rates by use of a high-speed video camera and comparison of these results against those measured by monitoring the change in pressure of the strand burner. The use of simultaneous burning rate measurements also compared the burning rate results for two different sources of aqueous HAN to further validate the accuracy of these measurements. Results of this investigation showed that aqueous HAN combustion results in two-phase burning where the liquid and gas phases are separated in the pressure trace by an inflection point in the rate of increasing pressure produced by the burning propellant. The method of burning rate measurements by the change in pressure was modified to use this inflection point as a point of propellant burnout, rather than the point of maximum pressure. By doing this, it was verified that either this

inflection point method or the high-speed video method could be used to measure the liquid phase burning rate of aqueous HAN, but also indicated that the gas phase produces significant exothermic reactions. A second burning rate measurement for HAN is defined by use of the peak pressure to capture the complete combustion of aqueous HAN and its two-phase burning behavior. An experiment to detect the presence of the hydroxyl radical as an intermediate combustion species in this gas phase reaction was also performed, which resulted in no evidence of its presence in either phase of aqueous HAN combustion.

# ACKNOWLEDGMENTS

First of all, I would like to offer my thanks to Dr. Eric Petersen for being an excellent advisor and educator to me these past years. His guidance has helped me tremendously as a student, an engineer, and as a scientist. I believe the opportunity that he has offered me to work with him while pursuing my Master's degree is truly unique, and I do not believe I would have been able to pursue a career in my ideal field had it not been for his support. I would also like to thank my committee members Dr. Sungyon Lee and Dr. Adonios Karpetis for serving on my committee and for being fantastic educators in the courses I have been fortunate to take with them.

I would also like to express my gratitude to the rest of my professors and mentors throughout my undergraduate and graduate studies, who have provided me with the knowledge and tools required so that I may become a successful engineer. Thank you also to my fellow researchers who have answered my questions, provided a helping hand, and have made a truly friendly and enjoyable research environment.

Most of all, I want to thank all of my family and friends who have provided encouragement and support all these years. To my parents who have constantly supported me and encouraged me to never stop dreaming, and my brother who always shows an interest in my work. Last of all, to my fiancée Tiffany Boobar, who has provided unconditional support and love for me all these years through countless late nights.

# CONTRIBUTORS AND FUNDING SOURCES

## Contributors

The work presented in this thesis was supervised by Dr. Eric Petersen, and was presented to the committee consisting of Dr. Sungyon Lee, and Dr. Adonios Karpetis. I would like to thank my entire committee for the assistance and feedback they have provided.

Special thanks are given to the Air Force Research Laboratory at Edwards Air Force Base, California for providing propellant samples to be studied. I would also like to acknowledge the help of Mr. Gabriel Homan-Cruz, who assisted me in conducting experiments for some of the data used in this presentation, particularly in collecting burning rate measurements. The remainder of the work presented in this thesis was conducted independently.

## Funding Sources

This work was supported in part by the Texas A&M Engineering Experiment Station and the TEES Turbomachinery Laboratory.

# NOMENCLATURE

| | |
|---|---|
| AFRL | Air Force Research Laboratory |
| FPS | Frames Per Second |
| GPIM | Green Propellant Infusion Mission |
| HAN | Hydroxylammonium Nitrate |
| HEHN | Hydroxyethylhydrazine Nitrate |
| Isp | Specific Impulse |
| J/kgK | Joules per Kilogram Kelvin |
| K | Degrees Kelvin |
| LED | Light-Emitting Diode |
| PFV | Photron Fastcam Viewer |
| TEAN | Triethanolammonium Nitrate |
| g | Grams |
| kV | Kilovolt |
| kΩ | Kilo-ohm |
| $m_b$ | Mass burned |
| mmHg | Millimeters of mercury |
| $m^3$ | Cubic Meters |
| mm | Millimeter |
| nm | Nanometer |
| MPa | Mega pascal |

| | |
|---|---|
| $\Delta t$ | Burn Duration |
| $h$ | Propellant Height |
| $ppm$ | Pixels Per Millimeter |
| $r$ | Burning Rate |
| $r_i$ | Burning Rate, Inflection Method |
| $r_v$ | Burning Rate, Video Method |
| $r_{pp}$ | Burning Rate, Peak Pressure Method |
| s | Seconds |
| $w_{r,i}$ | Measurement Error, Inflection Method |
| $w_{r,v}$ | Measurement Error, Video Method |
| wt. % | Percent by Weight |
| $X$ | Mole Fraction |

TABLE OF CONTENTS

Page

ABSTRACT ..... ii

ACKNOWLEDGMENTS ..... iv

CONTRIBUTORS AND FUNDING SOURCES ..... v

NOMENCLATURE ..... vi

TABLE OF CONTENTS ..... viii

LIST OF FIGURES ..... x

LIST OF TABLES ..... xii

1. INTRODUCTION ..... 1

1.1 Motivation for Current Study ..... 1
1.2 Overview of Thesis ..... 3

2. BACKGROUND LITERATURE REVIEW ..... 5

2.1 HAN-Based Propellant Formulations ..... 5
2.2 Aqueous HAN Burning Rate Experiments ..... 9

3. EXPERIMENTAL METHODS ..... 12

3.1 Strand Burner Overview ..... 12
3.2 Propellant Preparation and Ignition ..... 13
3.3 Peak Pressure Burning Rate Analysis ..... 15
3.4 High-Speed Video Burning Rate Analysis ..... 20
3.5 Modifications to the Existing Experimental Setup ..... 27
3.6 Error Analysis ..... 31

4. RESULTS AND DISCUSSION ..... 33

4.1 Peak Pressure versus High-Speed Video ..... 33
4.2 Comparison of Different HAN Sources ..... 40
4.3 Two-Phase HAN Combustion ..... 46
4.4 Detection of the Hydroxyl Radical ..... 52

5. CONCLUSION ..... 58

5.1 Present Study....58
5.2 Future Investigations....59

REFERENCES....61

APPENDICES....65

Appendix 1 – Sample Holder Design 1....65
Appendix 2 – Sample Holder Design 2....66
Appendix 3 – Measurement Error Analysis....67
Appendix 4 – Burning Rate Measurements for Aqueous HAN....71
Appendix 5 – Adiabatic Flame Temperature Results from ProPEP 3....74

LIST OF FIGURES

Page

Figure 1 - Burning rate of HANGLY26 monopropellant, image taken from Chang and Kuo [26]. ..... 8

Figure 2 - Aqueous HAN combustion zones defined by Katsumi et al., image taken from Katsumi et al. [32]. ..... 11

Figure 3 - Strand burner sample holder, electrodes, and loaded quartz tube. ..... 13

Figure 4 - Nitromethane pressure trace at 7.99 MPa. ..... 17

Figure 5 - HAN pressure trace at 8.18 MPa. ..... 18

Figure 6 - Images taken from the full nitromethane burn. From left to right, t = 0, +1.167, +2.334, +3.501, +4.668, and +5.835s. ..... 21

Figure 7 - Images taken from the full aqueous HAN burn. From left to right, t = 0, +0.02, +0.04, +0.06, and +0.08s. ..... 22

Figure 8 - Frame-by-frame of nitromethane propellant ignition. From left to right, t -0.0334, t -0.0167, t = 0 seconds. ..... 23

Figure 9 - Frame-by-frame of aqueous HAN propellant ignition. From left to right, t -0.004, t -0.002, t = 0 seconds. ..... 23

Figure 10 - Burnout of nitromethane propellant. The rightmost frame is burnout. ..... 24

Figure 11 - Burnout of aqueous HAN propellant, with the region of interest highlighted. The rightmost frame is burnout. ..... 25

Figure 12 - Coordinate selection for high-speed video method. ..... 26

Figure 13 - Example image from high-speed video. ..... 30

Figure 14 - Plot of nitromethane burns comparing the results for both methods with previous research. ..... 34

Figure 15 - Plot of Sigma Aldrich aqueous HAN burns comparing the results for both methods. ..... 35

Figure 16 - HAN pressure trace showing the time of ignition with the video burnout time superimposed. ..... 37

Figure 17 - Plot of HAN burning rates by use of the inflection point. ..... 38

Figure 18 - High-speed video versus inflection point burning rate measurements for 82.4 wt. % Sigma Aldrich HAN. ..... 39

Figure 19 - Comparison of Sigma Aldrich prepared aqueous HAN burning rates against Katsumi et al. [32]. ..... 41

Figure 20 - High-speed video versus inflection point burning rate measurements for 82 wt. % AFRL HAN. ..... 43

Figure 21 - Comparison of AFRL HAN, Sigma Aldrich HAN, and Katsumi et al. [32]. ..... 44

Figure 22 - Comparison of inflection point burning rates at pressures greater than 5 MPa. ..... 45

Figure 23 - Presence of opaque gas inside of the quartz tube during the time of continued increase in pressure beyond the inflection point. ..... 47

Figure 24 - Pressure rise comparison between the inflection point and the peak pressure for both HAN sources. ..... 48

Figure 25 - Two phase burning rate measurements via the peak pressure method. ..... 52

Figure 26 - OH* produced by combustion of nitromethane at 8.6 MPa with a solid propellant booster ignition. ..... 54

Figure 27 - OH* produced by steady nitromethane burning. ..... 55

Figure 28 - Voltage output of photomultiplier versus pressure trace for aqueous HAN at 7.38 MPa. ..... 56

Figure A5.1 - ProPEP 3 results for adiabatic flame temperature versus test pressure for 82.4 wt. % aqueous HAN. ..... 74

LIST OF TABLES

Page

Table 1 - Composition of HAN-based liquid gun propellants [21].....6

Table 2 - Formulations used by Wucherer and Christofferson [18].....7

Table 3 - Aqueous HAN solutions tested by Vosen [30].....9

Table 4 - Density of tested propellants.....19

Table 5 - Mass of water required to be vaporized to produce the change in pressure between the inflection point and the peak pressure.....50

Table 6 - Various configurations of OH* detection for aqueous HAN.....56

Table A3.1 - Measurement error for the inflection and high-speed video burning rates. 68

Table A4.1 - Burning rate measurements for liquid phase aqueous HAN and corresponding errors. .....71

Table A4.2 - Burning rate measurements for two-phase aqueous HAN and corresponding errors. .....72

# 1. INTRODUCTION

## 1.1 Motivation for Current Study

Liquid monopropellants have been used extensively in the field of rocket propulsion as a means of primary propulsion, attitude control, and powering turbomachinery used in large liquid bi-propellant engines [1], [2], [3]. Despite their low specific impulse when compared to other rocket propellants, liquid monopropellants are highly desirable because of their simple propellant-feed system [2], [4], which is typically accomplished by use of an inert pressurized gas. While there have been a variety of monopropellants investigated over the years, including hydrogen peroxide and various nitrate-based mixtures [1], hydrazine ($N_2H_4$) has been by far the most commonly used monopropellant. Hydrazine is a versatile chemical rocket propellant, capable of being used as a monopropellant in its most basic form, or as a bipropellant fuel in its derivative forms. Because of its extensive use for several decades, hydrazine-based monopropellant thrusters are very well developed, offering reliable performance and predictable behavior, which are critical traits for propulsion systems [5].

While hydrazine is highly desirable for its in-flight applications, it poses a risk to ground operations due to its health and environmental hazards. Hydrazine is harmful to the environment, highly toxic, and carcinogenic, requiring expensive and time-consuming ground operations to take a variety of precautions [6], [7], [8], [9]. Because of these potential health hazards to operators and the significant ground operation costs associated with the necessary precautions, alternative monopropellants to hydrazine are being pursued [1], [6], [7], [8], [9], [10], [11].

Several monopropellant candidates which have been investigated to replace hydrazine utilize the chemical hydroxylammonium nitrate (HAN), $NH_3O$-$HNO_3$. HAN, which may also be referred to as hydroxylamine nitrate, is an inorganic salt derived from hydroxylamine and nitric acid. Similar to hydrazine, HAN is a versatile chemical in the field of chemical rocket propulsion. It may be used as a monopropellant in an aqueous solution, or as an oxidizer in hybrid rockets [12], [13]. HAN-based monopropellants typically combine HAN with other constituents to improve its properties as a monopropellant. Because HAN is an oxygen-rich fuel and oxidizer blend, these added constituents are typically additional fuels to bring it closer to stoichiometry to improve performance, as well as the addition of water to reduce the flame temperature of the blend [14], [15]. The major combustion products of HAN also do not pose any risk to health or the environment, with water, molecular nitrogen, and molecular oxygen making up almost the entirety of the combustion products (> 99.99%). However, there may be traces of nitric oxide and nitrogen dioxide as a result of incomplete combustion.

An additional benefit of HAN-based monopropellants is a higher specific impulse density, lower freezing points, low vapor pressure, and high thermal stability when compared to hydrazine [1]. Despite all of the benefits that HAN has to offer, there are still several challenges which need to be overcome to justify the use of HAN-based monopropellants over the reliability which hydrazine offers. This set of challenges includes improvements to ignition and catalyst beds [16], [17], [18], [19], material compatibility issues, combustion instabilities, high burning rates, and high flame temperatures [17]. Improving the fundamental understanding of HAN's combustion

properties may help to resolve the issues relating to combustion instabilities, high burning rates, and high flame temperatures. All of these will help to advance the technology readiness level of HAN-based monopropellants for the purpose of replacing hydrazine.

## 1.2 Overview of Thesis

The purpose of this thesis was to improve the understanding of the combustion properties of HAN by performing fundamental combustion experiments with HAN in its most basic form as an aqueous solution. The primary property which was investigated is the burning rate of aqueous HAN over a range of pressures. To verify the accuracy of these experiments, the development and validation of a method of measuring burning rates of liquid monopropellants by use of a high-speed video camera was done. The results from this method were then compared to burning rate measurements by monitoring the change in pressure of the strand burner. Due to the two-phase burning behavior of HAN, additional experiments were performed in an effort to explain the causes of this behavior. These additional tests included burning rate experiments comparing the burning rates of HAN from two different sources to verify the same results, and measuring the hydroxyl radical in this gas phase of HAN combustion. To fully capture the two-phase burning behavior of HAN, a second burning rate measurement was defined to represent the complete combustion of aqueous HAN by incorporating the gas-phase reactions produced by the liquid-phase combustion products.

The second chapter of this thesis provides a background literature review of HAN. This review details the history and future of HAN as a propellant, as well as

investigations into aqueous HAN combustion behavior by other research groups. The third chapter details the experimental methodology used in this study, including descriptions of the experimental hardware and its configuration, propellant preparation, measurement techniques, and the error analysis. Chapter four presents the results and observations of the study then discusses what may be concluded as a result of this investigation. Finally, chapter five summarizes the results of this study, and proposes future investigations which would provide additional answers in understanding the combustion characteristics of aqueous HAN.

# 2. BACKGROUND LITERATURE REVIEW

## 2.1 HAN-Based Propellant Formulations

Although serious efforts into the use of HAN as a replacement for hydrazine have occurred only over the past two decades, its use as a propellant began with research into liquid gun propellants by the United States Army Ballistic Research Laboratory. The motivation of a liquid propellant gun is its theoretical benefits of caseless ammunition, increased muzzle velocity, and improved logistics [20]. Although experiments with HAN-based aqueous solutions were conducted by the U.S. Army, the concept of its use as a liquid gun propellant was first proposed by the Naval Ordnance Station in Indian Head, Maryland [20].

The early candidates of HAN-based liquid gun propellants are identified as LP-1845 and LP-1846, which was later reclassified as XM46. Both of these propellants are mixtures composed of aqueous HAN with triethanolammonium nitrate (TEAN) [21] as a tertiary amine fuel. The composition of these fuels can be seen in Table 1. Experiments with these propellants included burning rate measurements by recording the pressure in a closed chamber [22], and by visual methods via a windowed chamber [23], [24], [25]. Research was also done to investigate an issue of pressure oscillations seen in the combustion of both LGP-1845 and LGP-1846, which was resolved by increasing the burning rate of the propellant through the partial replacement of TEAN by the nitrate salt of N, N-diethylhydroxylamine (DEHAN).

**Table 1 - Composition of HAN-based liquid gun propellants [21].**

| Propellant Name | HAN (wt. %) | Water (wt. %) | TEAN (wt. %) |
|---|---|---|---|
| LGP-1845 | 63.2 | 16.8 | 20 |
| LGP-1846 (XM46) | 60.8 | 20.0 | 19.2 |

Further studies into a variety of fuel candidates to be combined with aqueous HAN were conducted by Wucherer and Christofferson. These fuel candidates included methanol, ethanol, hydroxyethylhydrazine nitrate (HEHN), and glycine [18]. All of these components are compatible and soluble in the aqueous HAN solution and improve the performance of the propellant, although both methanol and HEHN still pose toxic disadvantages. Wucherer and Christofferson conducted performance tests of HAN with these fuels in a small catalytically ignited rocket thruster. The formulations of the propellants used and their calculated performance for their experiments are seen in Table 2.

Wucherer and Christofferson were able to conclude from their experiments that high-performing HAN monopropellants could be formulated which are safe, storable, and can be ignited by a catalytic reactor. It was also found that the two propellants with the highest calculated specific impulse, HAN284MEO and HAN278HEH, containing methanol and HEHN, respectively, were both capable of performing well above hydrazine.

**Table 2 - Formulations used by Wucherer and Christofferson [18].**

| Designation | Specific Impulse (s) | Chamber Temperature (F) | Density ($g/cm^3$) |
|---|---|---|---|
| HAN250GLY | 250 | 3208 | 1.513 |
| HAN264GLY | 264 | 3607 | 1.575 |
| HAN269MEO | 269 | 3504 | 1.417 |
| HAN284MEO | 284 | 3900 | 1.392 |
| HAN253MEO | 253 | 2644 | 1.256 |
| HAN278HEH | 278 | 3807 | 1.483 |
| HAN271ETO | 271 | 3577 | 1.396 |

Another solution of HAN monopropellants is known as HANGLY26, a formulation consisting of 60% HAN, 14% glycine, and 26% water by weight. Burning rate measurements for HANGLY26 were conducted by Chang and Kuo [26] in a liquid propellant strand burner at pressures ranging from 1.5 to 14.5 MPa. Chemical analyses of the residual combustion products were performed by a gas chromatograph and a mass spectrometer. In their burning rate analysis, they found that there were four separate burning rate regimes, separated by a point break in the slope, as seen in Figure 1.

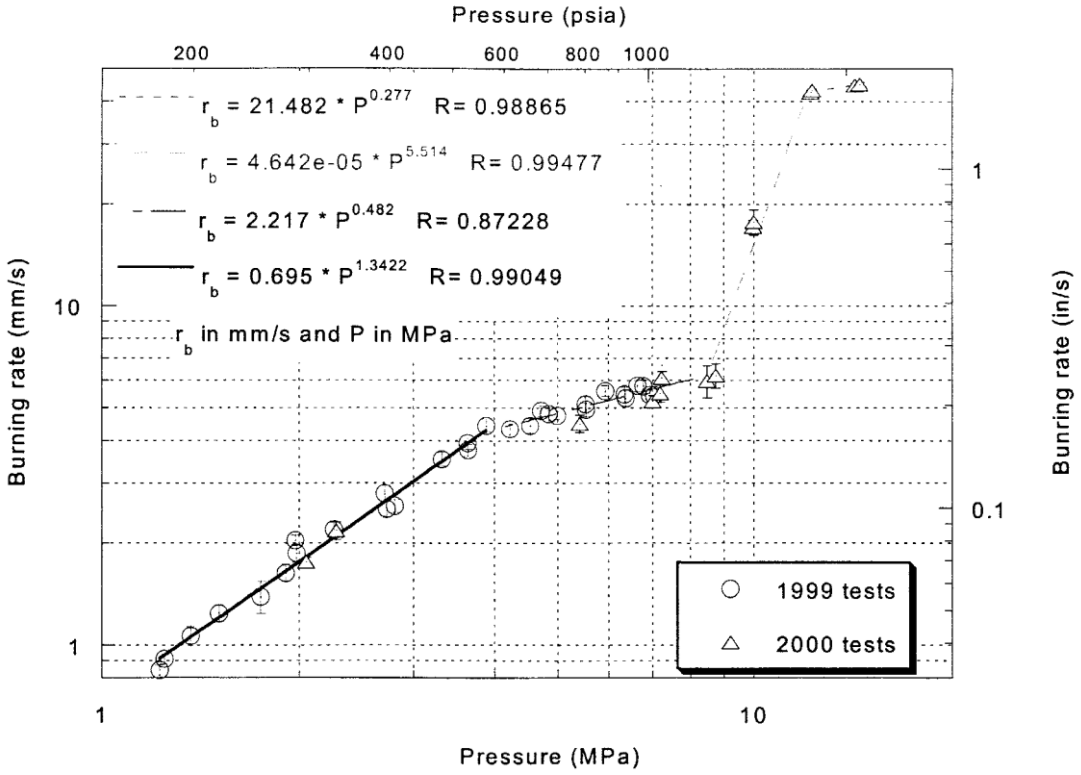


**Figure 1 - Burning rate of HANGLY26 monopropellant, image taken from Chang and Kuo [26].**

The HAN-based monopropellant of primary interest in recent years is the Air Force formulated AF-M315E. AF-M315E offers a number of benefits over hydrazine, including a 12% higher specific impulse (Isp), +50% specific impulse densities over hydrazine, a low minimum temperature threshold, and no freezing temperature due to its glass transition [9]. This results in potential improved spacecraft performance and safer ground operations. Although AF-M315E has yet to fly on any spacecraft, thruster and propulsion technologies have been and are continuing to be tested for AF-M315E to be used in the upcoming Green Propellant Infusion Mission (GPIM) [9], [27], [28], [29].

### 2.2 Aqueous HAN Burning Rate Experiments

Decomposition rate measurements for aqueous HAN mixtures, LGP-1845, and for LGP-1846 were conducted by Vosen and published in the late 1980s and early 1990s [25], [30], [31]. Vosen conducted the experiments in a constant-pressure strand burner over a test pressure range of 6 to 34 MPa, using visual burning rate and decomposition rate measurements from cameras to compile the data. In all of these experiments, ignition of the propellant was achieved by an electrical capacitive discharge. The concentrations of HAN in the aqueous solution used by Vosen ranged from 3.1 molar HAN to 13.0 molar HAN. The converted weight percentages which were calculated by Vosen's reported densities are shown in Table 3.

**Table 3 - Aqueous HAN solutions tested by Vosen [30].**

| Mixture | Density ($g/cm^3$) | HAN Wt. % |
|---|---|---|
| 3.12 M HAN | 3208 | 26.3 |
| 5.2 M HAN | 3607 | 40.7 |
| 7.02 M HAN | 3504 | 51.7 |
| 9.10 M HAN | 3900 | 63.1 |
| 11.05 M HAN | 2644 | 69.0 |
| 13.0 M HAN | 3807 | 86.9 |

While the 3.12 M HAN was unable to sustain decomposition, Vosen was able to conclude that the 5.2 M, 7.02 M, and 9.10 M aqueous HAN solutions produced a decrease in their decomposition rates with an increase in pressure up to 13 MPa. For pressures greater than 13 MPa, the decomposition rate appeared to be independent of pressure. It was also seen that the decomposition rates increased with the increasing concentration of HAN for the 5.2 M, 7.02 M, and 9.10 M mixtures. The 11.05 and 13.0 M HAN mixtures alternatively generated a decrease in decomposition rates with the increase in pressure throughout the entire test pressure range. Vosen also observed a difference in behavior of the decomposition front of the propellant for varying pressures. A corrugated decomposition front with no mean curvature was observed in high-pressure tests, while a distorted corrugated front with a large surface area was seen in low-pressure tests. Vosen suggested that this increase in surface area was a result of the hydrodynamic instabilities of the propellant and resulted in larger burning rates because of these pronounced hydrodynamic forces.

Toshiyuki Katsumi et al. performed burning rate experiments to better improve the combustion characteristics of aqueous HAN [32]. Katsumi et al. used an ignition wire to ignite a variety of aqueous HAN solutions, and they measured the burning rates by a medium-speed video camera at a frame rate of 500 frames per second (FPS); they measured the temperature of the propellant by type-R thermocouples. By combining the burning rate measurements, high-speed images, and temperature measurements, Katsumi et al. were able to propose a combustion wave structure of aqueous HAN. These results were also used to define the burning rates of HAN into three different zones, depending

on the concentration of HAN and the test pressure. These separate zones are shown by an image from Katsumi in Figure 2.

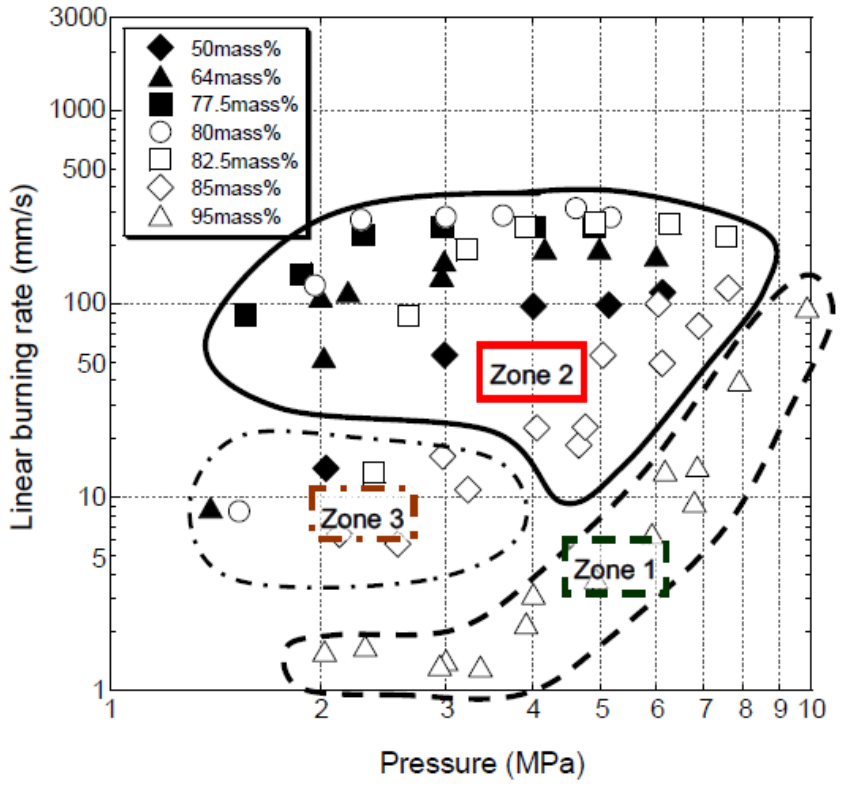


**Figure 2 - Aqueous HAN combustion zones defined by Katsumi et al., image taken from Katsumi et al. [32].**

The wave structure of Zone 1 was defined to be layered, and reactions occur in the gas phase. Zone 2 was stated to have liquid and gas phases, or a two-phase reaction zone. The high burning rates in Zone 2 were caused by rapid nucleation by superheating of the water in the aqueous solution. Meanwhile, the Zone 3 wave structure had alternating high and low burning rates. In this investigation, Katsumi et al. were also able to incorporate the hydrodynamic instability observed by Vosen into their combustion wave structure.

# 3. EXPERIMENTAL METHODS

## 3.1 Strand Burner Overview

Strand burners are useful tools in the field of chemical propellant combustion and are commonly used to test the combustion properties of rocket propellants. They are relatively simple in design, typically consisting of a cylindrical body with end caps, and serve a critical role in providing a safe method of containing burning propellant samples at high pressures. For data acquisition, they are often fitted with threaded ports and optical windows so that a variety of instrumentation probes or optical diagnostic techniques may sample the combustion environment inside of the vessel.

At Texas A&M University, a constant-volume strand burner is used which is capable of withstanding pressures up to 35 MPa. The internal dimensions of the strand burner are 94 mm in diameter, with a height of 203 mm. The strand burner is sealed on both ends by two large, hexagonal end caps. The body of the strand burner is fitted radially with three optical ports. Two of the optical ports feature sapphire windows which are used for high-speed video, emitted light measurements, and/or visible and near-infrared spectroscopy. The remaining port is fitted with a stainless steel plug and is used as a fill port for the pressurized gases.

The top end cap features another optical port with a sapphire window, which is used for laser ignition of propellants by a $CO_2$ laser, although this method is not used in this study. There is also plumbing fitted to this end cap which is used to depressurize the strand burner. The bottom end cap contains a hole where a propellant sample is introduced into the strand burner by the strand burner sample holder. This sample holder

is a modified screw which contains two electrodes to be used for igniting the propellant samples by a nichrome wire. One electrode is an insulated copper power lead which runs through the entire length of the sample holder. The other electrode is welded onto the sample holder body, which then grounds onto the entire strand burner vessel once the sample holder is inserted into the strand burner. Between the two electrodes is a 6.35 mm diameter hole with a depth of 6.35 mm. A quartz tube with an internal diameter of 7 mm is sealed on one end by a polytetrafluorethylene (PTFE) plug which is mounted into this hole to be used as a vessel to contain the liquid monopropellant sample. A graphic of the strand burner sample holder and quartz tube loaded with example amber liquid is seen in Figure 3.

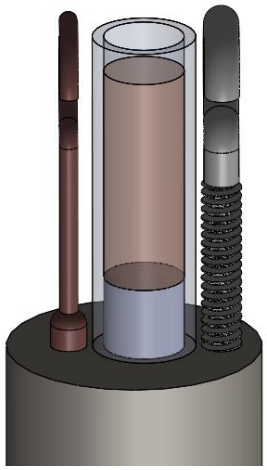

**Figure 3 - Strand burner sample holder, electrodes, and loaded quartz tube.**

### 3.2 Propellant Preparation and Ignition

Two different sources of HAN were used in this study. The first source was purchased from Sigma-Aldrich Co. in a 24 percent by weight (wt. %) aqueous solution, and the second was provided by the Air Force Research Laboratory (AFRL) at the

Edwards Air Force Base in California in an 82 wt. % aqueous solution. Previous aqueous HAN studies at Texas A&M have used HAN concentrations of 82.4 wt. %, which resembles typical concentrations used by other groups [32] and is similar to the concentration of available HAN [18]. For these reasons, this concentration was again used in the present investigation for comparison purposes.

It was decided to leave the AFRL-supplied HAN unaltered for this investigation since its concentration is very close to the desired 82.4 wt. %. However, the Sigma-Aldrich Co.-supplied HAN would need to be placed under vacuum in a desiccator for several days to evaporate excess water and increase the concentration of HAN in the solution. Due to the low vapor pressure of HAN, it was assumed that all of the mass lost in the evaporation process was water. This measured mass loss of water from the vacuum process was used to determine the new concentration of HAN. Once this concentration was greater than 82.4 wt. %, additional 24 wt. % solution HAN was added to the solution such that the concentration was reduced to the desired 82.4 wt. %.

Several additional experiments involved the use of neat nitromethane ($CH_3NO_2$) as a monopropellant, which was purchased from Sigma-Aldrich Co. at a purity $\geq$ 99.0%. Nitromethane served as an excellent baseline monopropellant for this investigation because of its low cost, low toxicity, and ease of storage. Furthermore, nitromethane has a very predictable burning rate at a known pressure, making it a good monopropellant to verify accurate burning rate measurements. Burning rate measurements of neat nitromethane have previously been investigated at Texas A&M by Warren [33].

The ignition source for the propellants is a 1-mm nichrome wire attached to the electrodes on the strand burner bolt. For a typical experiment, the nichrome wire is bent in such a way that once the propellant is loaded into the quartz tube via a bulb pipette, the wire will be suspended just below the surface of the propellant. A 6.0-Amp current at 18.0 Volts is sent through the wire by a switch relay from the safety of a control room. For nitromethane tests at pressures less than 4.5 MPa, the nichrome wire often failed to ignite the nitromethane. For nitromethane tests at these lower pressures, a small amount of solid propellant booster (80% mono-modal ammonium perchlorate/hydroxyl-terminated polybutadiene) was attached to the nichrome wire and rested above the surface of the nitromethane. The combustion of the solid booster provided enough heat to ignite the nitromethane without affecting its burning rate [34]. For the nitromethane tests, the strand burner vessel was partially pressurized with air to provide enough oxygen to sustain combustion, while the remainder of the pressurization was achieved by argon. For aqueous HAN tests, pressurization was achieved by argon.

### 3.3 Peak Pressure Burning Rate Analysis

By measuring the change in pressure of the constant-volume strand burner vessel which contains a combusting propellant sample, the duration of the propellant burn can be determined. This technique has been used at Texas A&M University before to measure the burning rate of liquid monopropellants [33], [35] and has proven to be a reliable method in the present investigations.

The pressure of the strand burner vessel is monitored by an OmegaDyne PX021C1-7.5KG5T pressure transducer. The data from the transducer is captured by a

computer-based oscilloscope board purchased from Gage operating with GageScope software. The GageScope software records the instantaneous readings of the transducer for 10 seconds (s) at a sampling rate of 1 kHz. The ignition of propellant caused a spike in pressure inside of the vessel which was seen in the pressure trace of the transducer, which in turn was used to determine the ignition time of the propellant sample. The pressure eventually reached a peak pressure and then began to slowly decrease. The point of time where peak pressure was achieved was used as the end time, or burnout, of the propellant. With the ignition time and burnout time of the propellant burn, the propellant burn duration, $\Delta t$, can be determined. The average of the pressure at the ignition time and the maximum pressure at burnout was recorded as the test pressure for that sample. Figures 4 and 5 show examples of typical pressure traces for both nitromethane and HAN at similar test pressures, respectively.

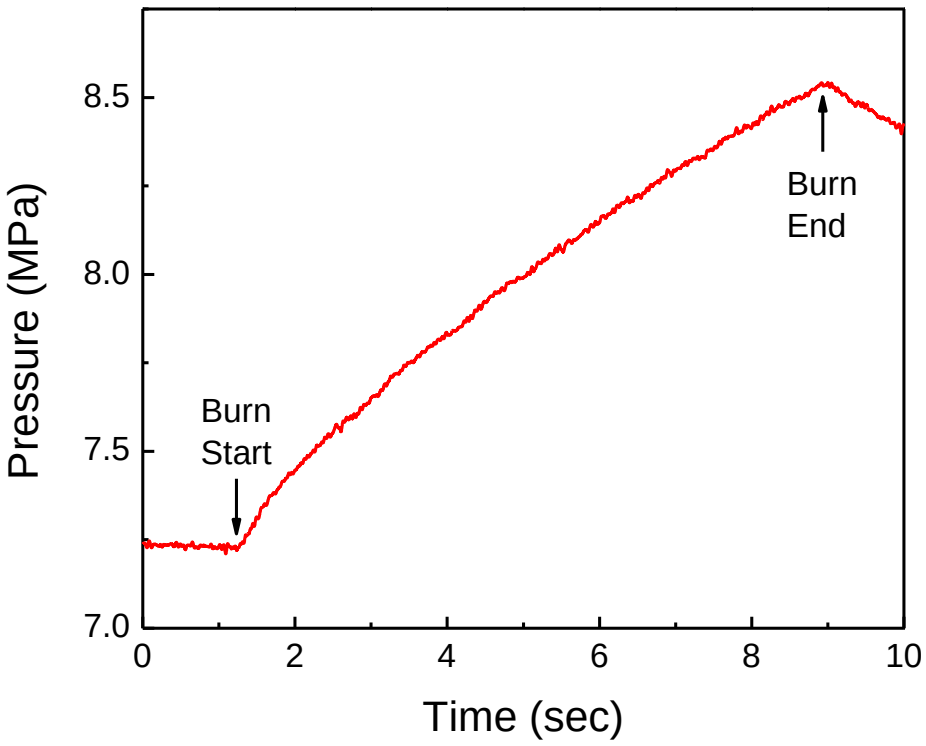


**Figure 4 - Nitromethane pressure trace at 7.99 MPa.**

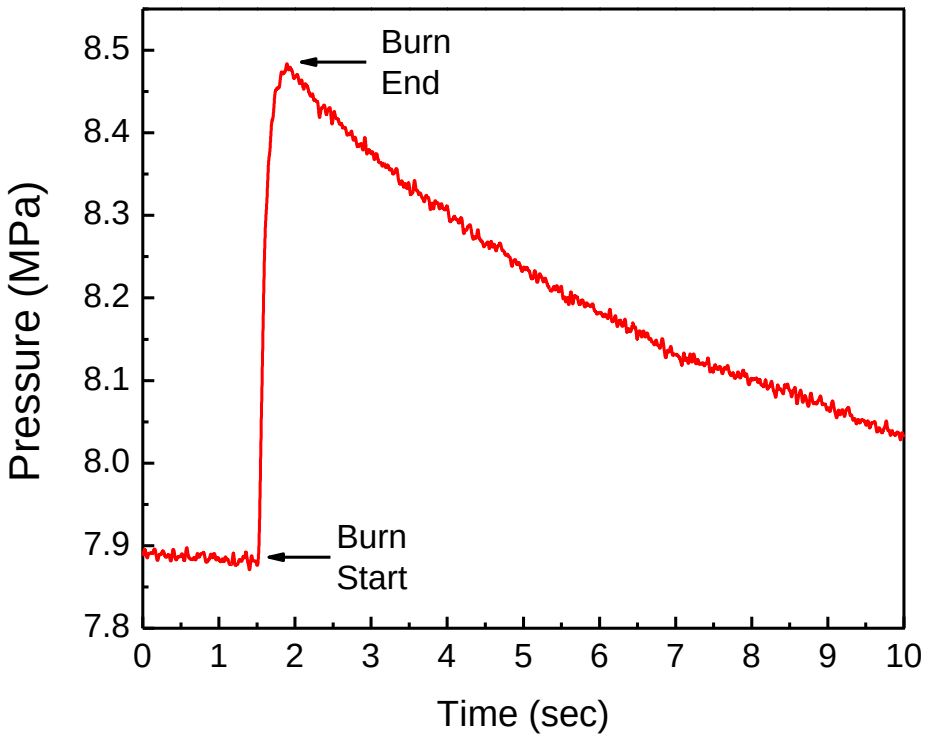


**Figure 5 - HAN pressure trace at 8.18 MPa.**

To determine the height of the propellant sample, *h*, the density of the propellant, the geometry of the quartz tube, and the mass of the propellant sample must be known. Before each test, the mass of the strand burner bolt which has been loaded with propellant is measured, and it is then measured again after the propellant has been burned. This difference in mass for these two measurements is used as the mass of propellant burned. Using the calculated and reported densities of the propellant, which are shown in Table 4, the volume of the propellant burned is calculated, and then can be converted to the sample height, *h*, using the known internal diameter of the quartz tube.

**Table 4 - Density of tested propellants.**

| Propellant Name | Density (g/cm$^3$) |
|---|---|
| Nitromethane | 1.138 |
| Sigma Aldrich HAN 82.4 wt. % | 1.545 |
| Air Force Research Laboratory HAN 82 wt. % | 1.536 |

Both the nitromethane and AFRL HAN densities were provided by the supplier. However, the Sigma Aldrich-supplied HAN density would need to be calculated as a result of the propellant preparation process discussed earlier. An equation was developed by Sassé [36] to calculate the density of aqueous HAN with a known weight %, and is shown in (1). This equation was used with the calculated 82.4 wt. % as a result of the evaporation process to determine the density of 1.545 g/cm$^3$. Verification of these densities at Texas A&M was also conducted by Gabriel Homan-Cruz [37] and was found to agree well with the results of (1).

$$\rho_{HAN/H_2O} = 1.00083 + 4.5813x10^{-3}(wt\%\ HAN) + 2.4609x10^{-5}(wt\%\ HAN)^2 \quad (1)$$

With the burn duration, $\Delta t$, and sample height, $h$, the linear burning rate for the propellant, $r$, can be calculated using (2).

$$r = \frac{h}{\Delta t} \quad (2)$$

### 3.4 High-Speed Video Burning Rate Analysis

High-speed video recordings of propellant burns are a commonly used technique in the study of propellant burning rates. This method allows the investigator to determine the time it takes for a propellant sample to burn along a known length observed by the high-speed video camera. The benefit of this method is that it allows for highly accurate time measurements, depending on the frame rate used in the recording. The higher the frames-per-second (FPS) count used in the recordings, the higher the accuracy in determining beginning and end times for the burning rate measurements. However, higher FPS counts often have a trade-off of lower image resolution and a darker image due to the reduced time of the shutter being open. Furthermore, high-speed cameras are often very expensive, and require an optical port for the camera to have a view of the experimental sample. Designing optical ports into high-pressure systems increases the cost of the system design, and it is the most likely point of failure in a high pressure system.

The high-speed video camera used for burning rate measurements at Texas A&M University is a Photron FASTCAM SA3 120K. The image of the camera is enhanced by a Nikon Micro-Nikkor 105mm f/2.8 lens; three extension tubes measuring 12, 20, and 36 mm; and a Nikon HS-14 Lens Hood. The Micro-Nikkor lens has a minimum aperture of f/32, and a maximum aperture of f/2.8. The resolution of the camera is dependent on the framerate being used. The camera is capable of recording at its maximum resolution of 1024 × 1024 at frame rates up to 2000 FPS. The maximum possible framerate is 120,000 FPS at a resolution of 128 × 16. The resolution and framerate have limiting effects on

the recording duration, which must be accounted for to capture the entire burn of a sample. The framerate used to measure the burning rate of nitromethane and aqueous HAN herein were 125 and 500 FPS, respectively.

The software used to manage the recordings and edit the videos is Photron FASTCAM Viewer (PFV). This software is used to adjust the settings of the camera, including the resolution, frame rate, and shutter speed. The image can also be adjusted using the software to alter the gamma, contrast, and brightness settings.

The technique developed for this study to measure the burning rate of liquid propellants by high-speed video is as follows. PFV is capable of selecting and navigating individual frames of the recorded video. By navigating through the individual frames of the propellant burn video, the beginning and end points of the propellant burn can be found. Figures 6 and 7 show several images over equal intervals respective to the time it takes for the particular propellant to completely burn. These images capture both the moments of ignition and burnout for nitromethane and aqueous HAN.

**Figure 6 - Images taken from the full nitromethane burn. From left to right, t = 0, +1.167, +2.334, +3.501, +4.668, and +5.835s.**

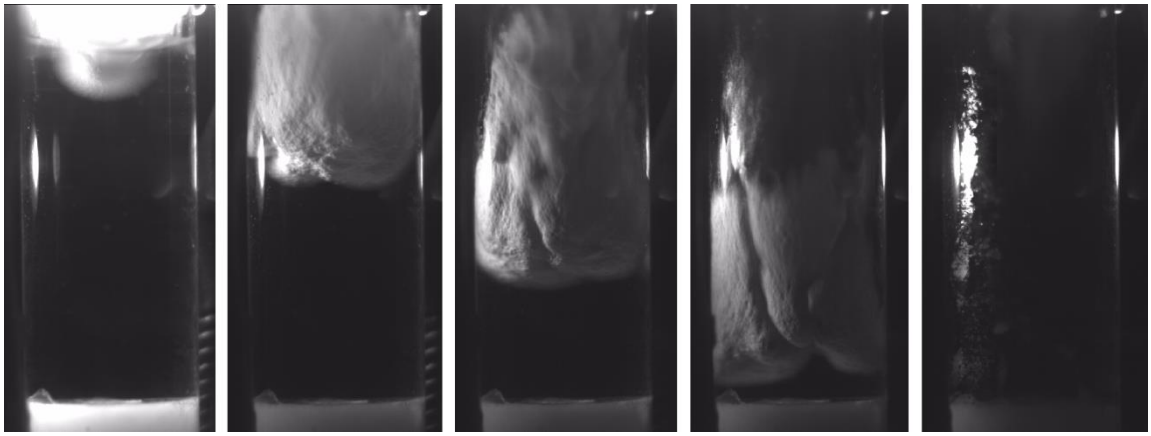

**Figure 7 - Images taken from the full aqueous HAN burn. From left to right, t = 0, +0.02, +0.04, +0.06, and +0.08s.**

To determine the point of propellant ignition, the region surrounding the nichrome wire was analyzed to find the frame number at which combustion activity can first be seen. For nitromethane, this combustion activity is observed as a sudden increase in brightness at the surface of the sample, indicating the presence of a visible flame which is soon followed by the regressing propellant front. For HAN, a bubble will appear at some point along the submerged section of the nichrome wire, which quickly grows in size. Examples for ignition of both nitromethane and HAN can be seen in Figures 8 and 9.

**Figure 8 - Frame-by-frame of nitromethane propellant ignition. From left to right, t -0.0334, t -0.0167, t = 0 seconds.**

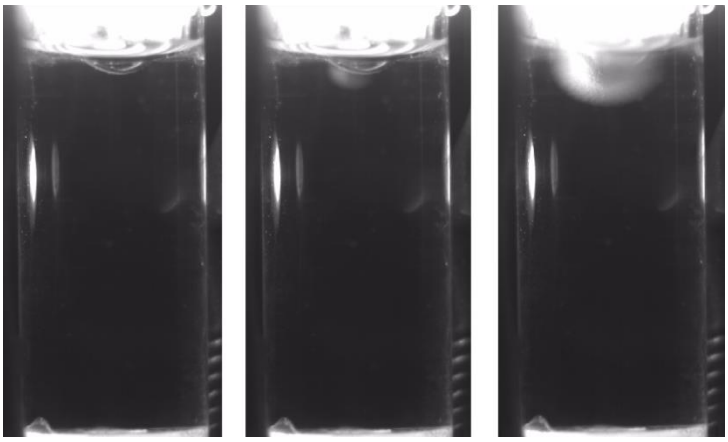

**Figure 9 - Frame-by-frame of aqueous HAN propellant ignition. From left to right, t -0.004, t -0.002, t = 0 seconds.**

A similar process to the method used to determine ignition is applied once more to determine the time of burnout by observing the bottom of the propellant sample to find the frame number at which combustion has stopped and burning is complete. For nitromethane tests, the frame where the visible flame has lifted from the bottom of the

quartz tube is used as the point of propellant burnout. The final frames leading to nitromethane burnout are seen in Figure 10.

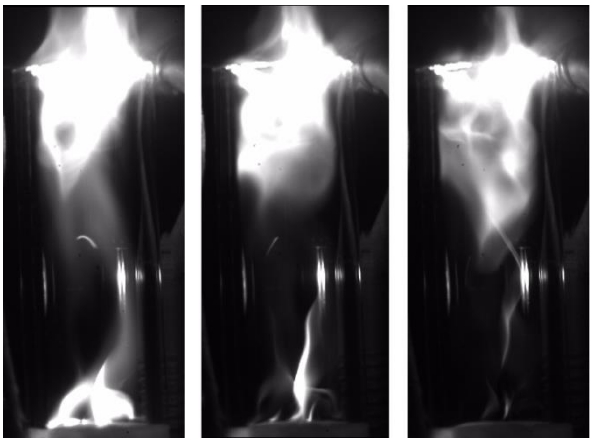

**Figure 10 - Burnout of nitromethane propellant. The rightmost frame is burnout.**

For HAN, this burnout point occurs when the liquid propellant has reached the bottom of the quartz tube, and there is no further movement of liquid in this region. Figure 11 shows the final five frames of the liquid burning of HAN, with the region of interest highlighted for clarity. The final frame is the frame where burnout is observed. It should be noted that the regression of the liquid propellant in this image is along the sidewall, rather than down the center of the quartz tube. This is common in aqueous HAN combustion tests, especially for high burning rate tests, and it is attributed to the same hydrodynamic forces seen by Vosen [30]. Because of this, the point where the entire liquid sample has burned is taken as the burnout point of the propellant rather than the point of time where the sample crosses a predetermined location.

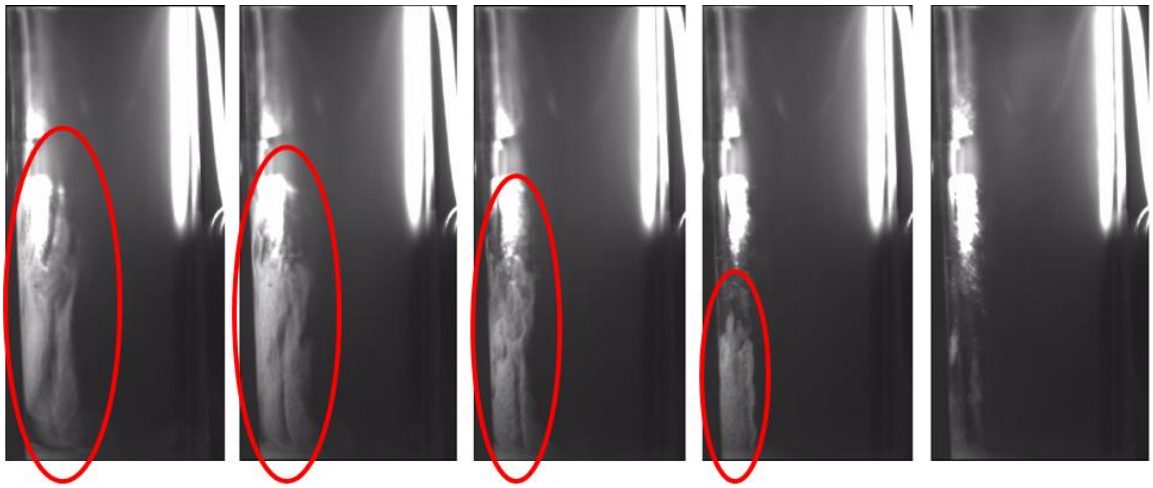

**Figure 11 - Burnout of aqueous HAN propellant, with the region of interest highlighted. The rightmost frame is burnout.**

By subtracting the initial frame number from the final frame number, the total number of frames corresponding to propellant burning can be determined. Then dividing this total number of frames by the corresponding FPS value used in the recording, the burn duration, $\Delta t$, is determined.

The PFV software also features a xy-coordinate tool which shows the x and y pixel coordinates of the mouse for the image in the recordings. This tool is very useful for the burning rate measurements because it provides a method of determining the height of the propellant sample being burned. To do this, a known length must be apparent in the image to determine a pixel-per-distance value. Once this value is known, the height of the propellant sample in pixels can be measured using the xy-coordinate tool and then converted into the height of the propellant in a unit of length. In this experiment, the known length is the outer diameter of the quartz tube which holds the propellant, which was measured by digital calipers to be 8.97 millimeters. This

conversion of height in pixels to height in millimeters is done for every burn recording. Figure 12 shows a single image of a recording and the various locations where the coordinates are taken to determine the height of the propellant sample.

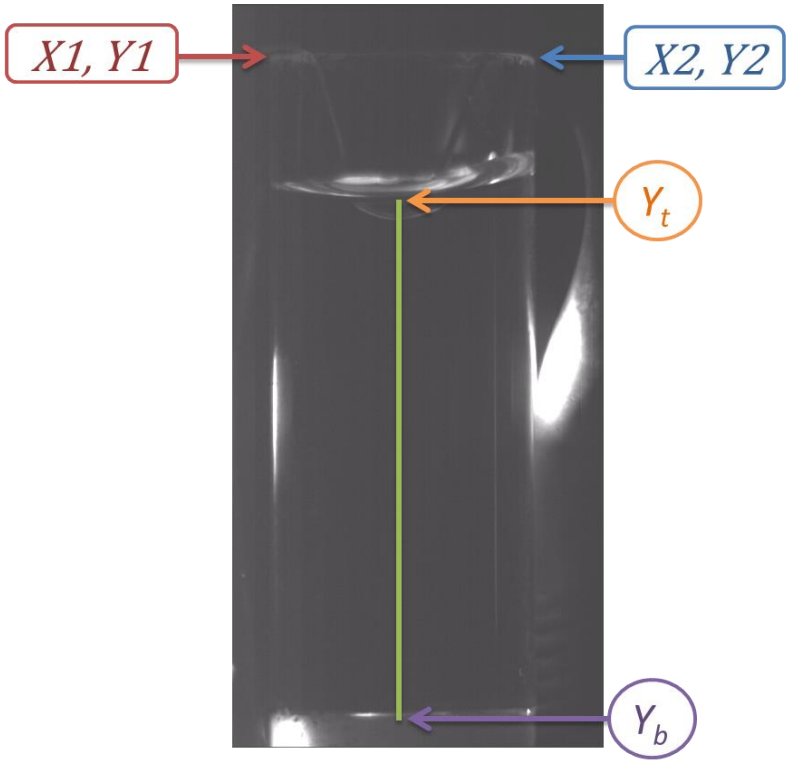


**Figure 12 - Coordinate selection for high-speed video method.**

The point coordinates $X_1$, $X_2$, $Y_1$, and $Y_2$ are used to calculate the pixels-per-distance value in units of millimeters. The two y-coordinates are included to account for any tilt in the quartz tube, and using the Pythagorean Theorem, the distance between $X_1$, $Y_1$ and $X_2$, $Y_2$ in pixels is determined. This value is then divided by the 8.97 millimeter diameter of the quartz tube to determine the pixels-per-millimeter value, *ppm*. This process is summarized in (3)

$$ppm = \frac{\sqrt{(X2 - X1)^2 + (Y2 - Y1)^2}}{8.97mm} \quad (3)$$

$X_t$ and $Y_t$ are determined by selecting the point as close to the meniscus as possible, similar to how a graduated cylinder is read. $X_b$ and $Y_b$ are selected as the point at the bottom of the quartz tube at the surface of the Teflon plug such that $X_b$ is the same as $X_t$. The difference in pixels between $Y_t$ and $Y_b$ creates a straight line measurement in pixels between the top and bottom of the propellant sample. This distance in pixels can then be converted to the propellant height, *h*, in millimeters using the calculated *ppm* from (3). This process is represented in (4).

$$h = \frac{Y_t - Y_b}{ppm} \quad (4)$$

With the burn duration, $\Delta t$, and propellant height, *h*, both known, the linear burning rate, *r*, of the propellant is determined by (2).

### 3.5 Modifications to the Existing Experimental Setup

To record videos of HAN burning, some modifications were necessary to the existing experimental setup. These modifications included machining a new sample-holder bolt to raise the height of the quartz tube such that it could be within line of sight of the high-speed video camera. This modification was necessary as the original sample holder bolt was not designed for liquid monopropellant experiments or high-speed video burning rate measurements. This new bolt was machined using carbon steel hex stock because no full-threaded bolts of this length were available at that time. This design may be seen in Appendix 1.

Another design was later created and used which included an O-ring face seal to improve the leak rate of the system, and this allowed higher pressure operations. This second bolt is similar in length to that of Appendix 1 but features a larger bolt head to accommodate a Buna-N O-ring. Due to availability, this sample holder was machined out of a full-thread bolt. This design may be seen in Appendix 2.

It was also necessary to introduce a light source into the strand burner vessel to illuminate the quartz tube sample holder to be seen by the high-speed video camera. This addition was necessary because aqueous HAN does not produce any visible light as it burns, unlike nitromethane and the solid propellants previously tested at Texas A&M. It should be noted that the light seen at the sample surface in some HAN tests is due to the incandescence of the nichrome wire and not from a visible flame. There were three requirements for selecting a light source for the system. First, it was necessary to select a wavelength of light which would not fall within the wavelength range of the photodetector. This wavelength discrimination was to prevent the introduction of a background signal which could saturate the photodetector data. Second, the light source needed to provide a sufficient amount of light to be able to see the surface of the liquid propellant sample inside of the quartz tube with the high-speed video camera. The inside walls of the strand burner vessel are typically coated in a film of soot from previous tests, which reflects almost no light and makes illuminating the sample more difficult. Last of all, because it was decided to insert the light source directly into the system rather than use another optical port, the light source needed to be able to operate in the high pressures of the strand burner vessel. Installing the light source inside of the vessel

prevents the loss of one of the optical ports and its respective instrument. This placement also allows for the light source to be much closer to the sample, which improves the lighting of the sample. This modification also required the light source to be small enough to fit inside of the strand burner vessel.

It was decided to use a 5-mm, 470-nm wavelength light-emitting diode (LED) with a 45-degree viewing angle from LED Supply. This LED is sufficiently small to be able to fit inside of the strand burner vessel, and the addition of a blue light filter prevented the 470-nm wavelength from saturating the near-infrared bandwidth used by the photodetector. It was presumed that the luminous intensity and viewing angle would be sufficient to light the sample, but trial runs were first necessary.

Research into the operating pressures of LEDs provided no conclusive results in regards to failure pressures or the effects of high pressures on the LED. Due to the inexpensive costs of these LEDs, it was decided to run tests to determine how well the LED could operate at high pressures. Before any test could be done, a power source for the LED was also added to the strand burner vessel. A variable power supply was connected to an insulated, two-wire power lead gland from Conax to power the LED. The current and voltage settings used were 0.15A and 3.2V.

To prevent having to machine the strand burner vessel to fit the power leads into the system, the power leads were instead routed through the inert gas fill lines. To do this, a Swagelok tee was introduced upstream of the fill port where the leads could feed through the tee and into the vessel with the LED soldered onto the leads. This solution

also ensured that the LED was aligned such that its light would fall directly on the sample since the optical ports are all aligned along the same plane.

To determine if the LED was capable of providing sufficient light to see the entire sample and the surface level of a liquid, the quartz tube was filled with water and loaded into the strand burner vessel at atmospheric pressures. With the LED on, and the lens aperture set to the maximum f/2.8, the surface level of the water could still be easily seen with the high-speed video camera at frame rates up to 500 FPS, as seen in Figure 13. At frame rates higher than this upper rate, it becomes difficult to distinguish the surface level of the sample, even after adjusting the brightness and contrast of the recording software.

**Figure 13 - Example image from high-speed video.**

To determine whether the LED could operate at high pressures, the empty sample-holder bolt was loaded into the system to seal the strand burner vessel so that it could be pressurized. The LED was monitored via a live feed of the high-speed camera for failure of the LED. The strand burner was pressurized initially to 3.45 MPa and

monitored for 5 minutes for any changes. The pressure was then increased by 1.72 MPa and monitored for an additional 5 minutes. This process was repeated until the final test pressure of 10.34 MPa was reached. Throughout the entire 25-minute duration, there were no apparent effects of the pressure on the LED as observed by the camera. After the system was vented and the LED removed, there also appeared to be no physical damage to the LED. The LED was determined to be capable of meeting the test pressure requirements. Later, unrelated experiments were also done where the LED was subjected to pressures reaching 35 MPa, and it was still capable of operating.

### 3.6 Error Analysis

To determine the error attributed to measurement uncertainty, a root-sum-square error analysis was performed for both the pressure method as well as for the high-speed video method. Results from this error analysis approach resulted in small errors, especially for the pressure method where sharp changes in pressure traces make well defined points for determining the beginning and end times. The results from this error analysis are found in Appendix 3.

Although it appears that the measurement uncertainty for the burning rates is quite low, the statistical uncertainty is a much greater factor in the scatter seen in the burning rate data. Therefore, a statistical error analysis was used rather than the measurement error analysis. In statistical uncertainty analysis, “random’ errors can have significant effects on experimental results. For aqueous HAN burning rate measurements, there is evidence supporting this suggestion of random errors which have been observed. Non-symmetric flame fronts, similar to what was seen by Vosen [30], can

greatly affect the burning rate by allowing higher mass flux decomposition due to the increased surface area, resulting in a higher burning rate. These non-symmetric flame fronts have been observed in high-speed videos, as detailed in section 3.4 of this thesis. Variations to the concentration of HAN and free nitric acid present in the solution also affect the burning rate of the propellants. Additionally, non-uniform preheating from the nichrome wire due to its relative location to the center of the quartz tube could also result in this statistical uncertainty.

The statistical error analysis was accomplished by sorting every test from smallest to lowest test pressure separately for both the high-speed video and pressure methods. Tests which were conducted within 0.25 MPa of each other were then binned together, where the mean, standard deviation, and standard deviation of the mean of the burning rates for that group were calculated. The standard deviation of the mean, or the standard error, was then calculated into a percent error for its respective bin. The average of the percent errors for every bin was then calculated and attributed as the percent error for the entire set of data, including those points which were not originally included in any bin. For the peak pressure method, this average percent error was found to be 14.22%; for the inflection pressure method which is discussed in the next chapter, this percent error was found to be 10.96%; and for the high-speed video method, this percent error was 11.88%. These percent errors were then factored in as error bars in the plots. The burning rate measurements and their calculated errors from this process are found in Appendix 4.

# 4. RESULTS AND DISCUSSION

## 4.1 Peak Pressure versus High-Speed Video

A validation experiment for the high-speed video method was necessary to determine its effectiveness in measuring the burning rate of the liquid monopropellants. This initial test measured the burning rate of neat nitromethane by both the high-speed video and the peak pressure methods simultaneously at test pressures of 5.53 MPa – 13.06 MPa. These burning rates were then compared to the burning rates measured by McCown by the peak-pressure method [33], whose values were found to agree with the burning rate measurements determined by Boyer and Kuo [38], as well as for Sabourin et al. [39]. The burning rates determined by both the high-speed video and the peak pressure method in this study agreed well with what was seen by McCown, indicating that the high-speed video method detailed herein is able to accurately measure the burning rate of neat nitromethane. The burning rate measurements for this comparison are seen in Figure 14.

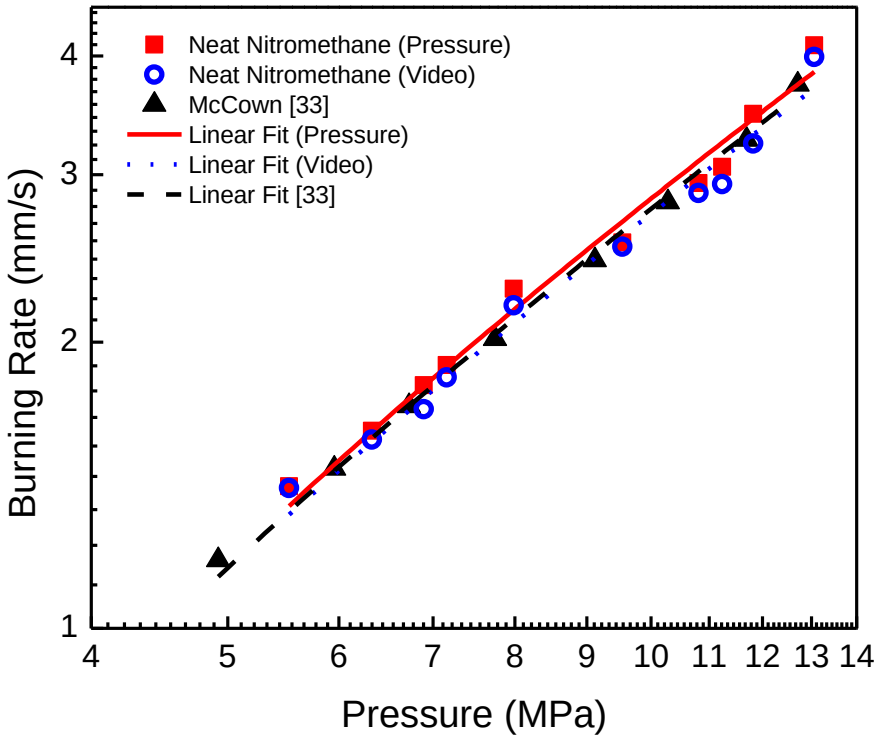


**Figure 14 - Plot of nitromethane burns comparing the results for both methods with previous research.**

Having proven that either the high-speed video method or the peak pressure method could be used to measure the burning rate of neat nitromethane, the same validation experiment for measuring the burning rate of the Sigma Aldrich-prepared aqueous HAN was done. An initial set of 5 experiments was done for a pressure range of 4.13 MPa to 8.30 MPa, and the results of this experiment are seen in Figure 15.

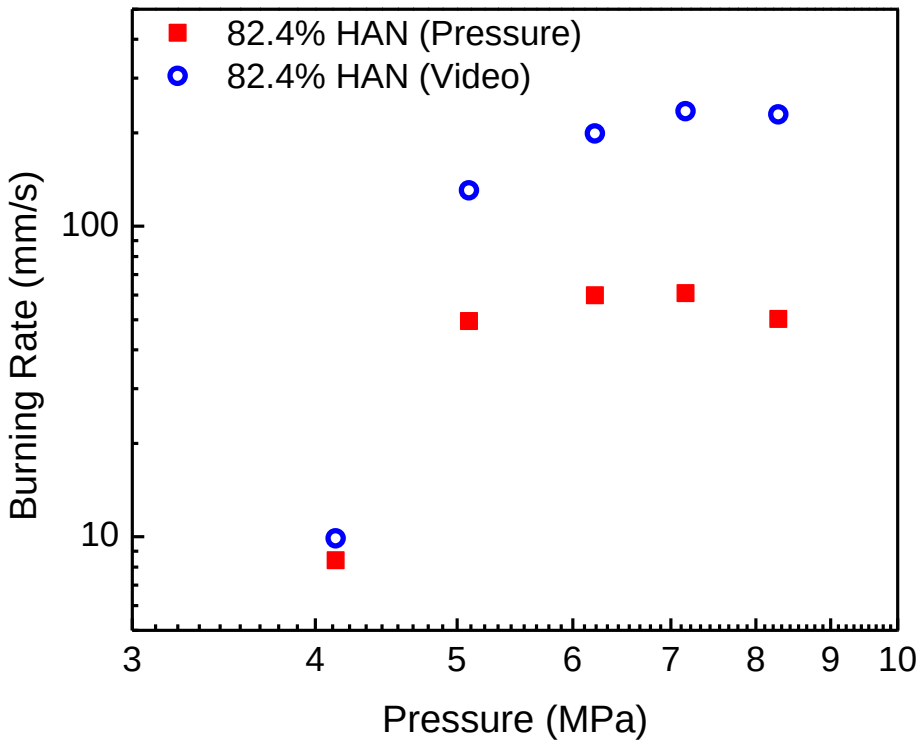


**Figure 15 - Plot of Sigma Aldrich aqueous HAN burns comparing the results for both methods.**

While the burning rate measured by both methods agreed well at the 4.13 MPa test pressure, the burning rates for test pressures greater than 5 MPa were drastically different. The burning rates measured by the high-speed video were orders of magnitude larger than what was measured by the peak-pressure method, well outside of any reasonable error analysis. This discrepancy seemed to indicate that unlike for neat nitromethane, the high-speed video method and peak pressure method could not be used interchangeably for measuring the burning rate of aqueous HAN.

Such a large difference in measured values cannot be explained by a fault in the measurement technique, rather it indicates that there may be some behavior that cannot be captured by only one method of burning rate measurement. The duration of the burn from the pressure trace indicates a burn time of the propellant that is much longer than what is seen in the video for when there is no more propellant left inside of the quartz tube. To find the cause in the difference between the values, the assumption was made that the start of combustion for the two methods is the same, and that the difference lies in determining the time of propellant burnout. The duration of the burn found by the video was superimposed on the pressure trace to analyze the pressure of the system at the time that the video data indicate that the burn was complete. The scale of time for the data analysis was reduced from ten seconds to two seconds to better see any unusual behavior which may be present in the pressure trace. A point was marked on the pressure trace where the video data indicated the end of the burn, as seen in Figure 16.

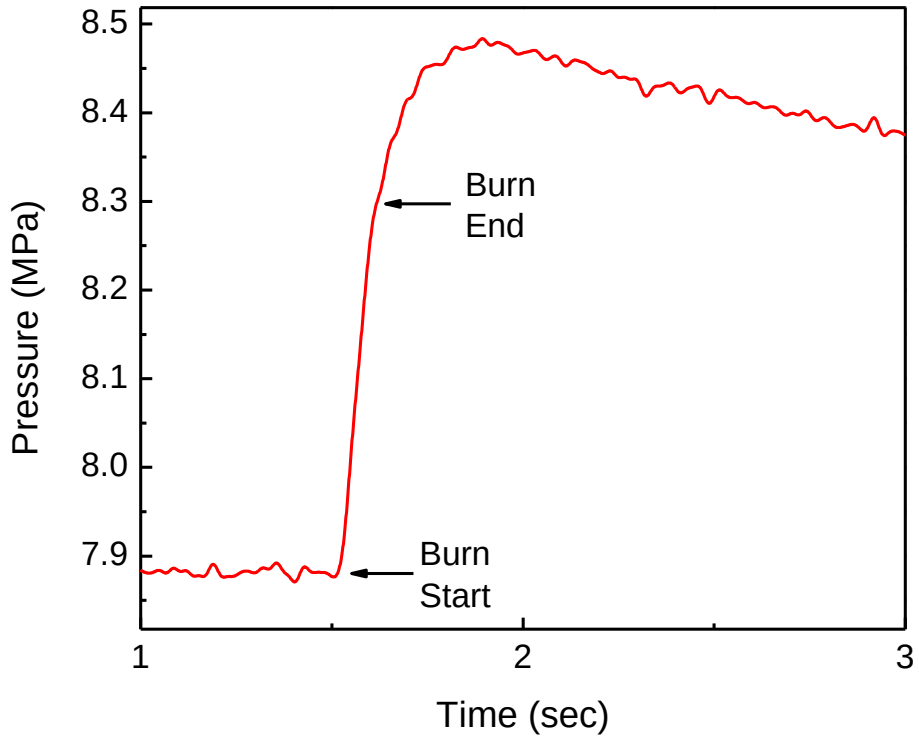


**Figure 16 - HAN pressure trace showing the time of ignition with the video burnout time superimposed.**

At the point of the pressure trace in Figure 16 marked “Burn End”, there is a noticeable change in slope of the pressure trace. The trace changes from a sharp linear increase in pressure to a more-rounded trace where the rate of increase in pressure continually decreases until it reaches the peak pressure some time later. This behavior is unlike any which has been observed in any other propellant tested before at Texas A&M, whether it is a liquid monopropellant or a solid propellant. Revisiting the pressure trace for the remaining of the aqueous HAN tests, this change in slope was also observed at test pressures greater than 5 MPa. The burning rate measurements by the pressure trace

were revisited by using this inflection point as the burn end time rather than the peak pressure point. To prevent biasing the data, the burn time of the video was not superimposed when revisiting the pressure trace data, and was instead done by looking for this inflection point in the pressure. These revisited pressure trace burning rates are shown in Figure 17.

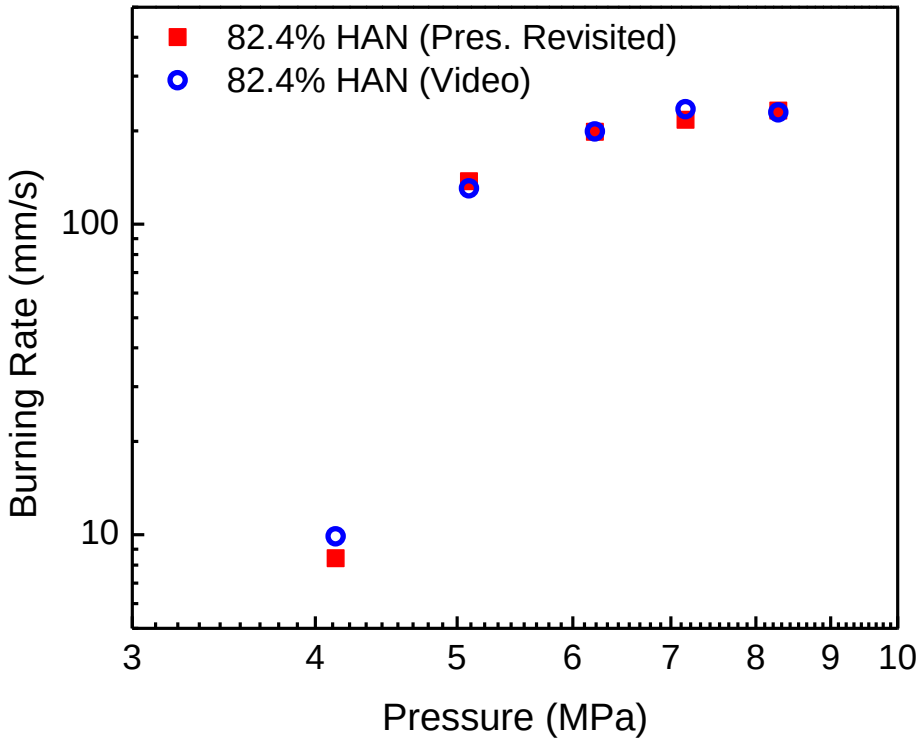


**Figure 17 - Plot of HAN burning rates by use of the inflection point.**

By using the inflection point of the pressure trace rather than the peak pressure for the aqueous HAN mixtures, the burning rate measurements between the two measurement methods once again agree with each other as they did for the nitromethane

experiments. Further burning rate measurement comparisons were done, and they required the preparation of several batches of aqueous HAN supplied from Sigma Aldrich. These different batches are labeled separately to observe any variances in burning rate which may be attributed to the preparation process of the Sigma Aldrich-supplied HAN. These various batches of HAN were tested over a range of pressures from 4 MPa to 15 MPa, and the results are shown in Figure 18. No tests were able to be performed at pressures below 4 MPa due to unreliable ignition of the aqueous HAN solutions at these pressures.

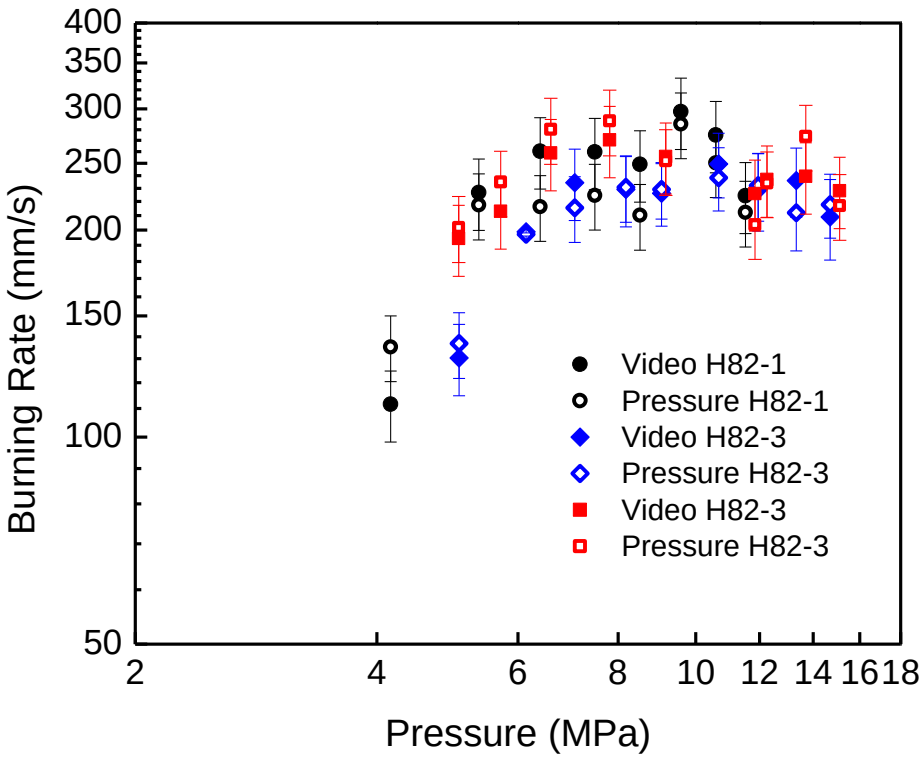


**Figure 18 - High-speed video versus inflection point burning rate measurements for 82.4 wt. % Sigma Aldrich HAN.**

Similar to what was seen in the Figure 17 comparisons, the burning rate measurements by high-speed video and by the inflection point of the pressure trace fall well within the error bars of one another for the same test, especially at higher test pressures where less scatter is seen. This agreement indicates that either method proves sufficient in measuring the burning rate of aqueous HAN for this test pressure range. It should be noted that while the two methods produce similar burning rate measurements for the same test, there does appear to be variance in the burning rate measurements across the different batches of the Sigma Aldrich-prepared solutions.

### 4.2 Comparison of Different HAN Sources

To determine which batch of the Sigma Aldrich-prepared HAN best represents the true burning rate of aqueous HAN, comparisons were done between data presented by other researchers and by conducting further experiments with a different source of aqueous HAN. The burning rates of the aqueous HAN measured by the inflection point were first compared against the 82.5 wt. % aqueous solution burning rates by Katsumi et al. [32], as seen in Figure 19.

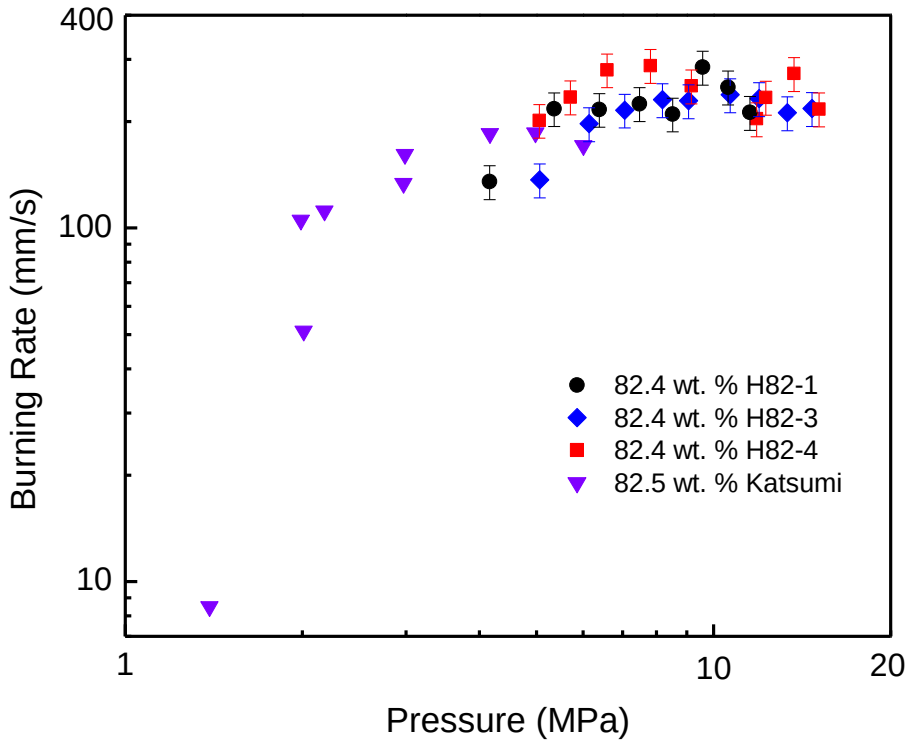


**Figure 19 - Comparison of Sigma Aldrich prepared aqueous HAN burning rates against Katsumi et al. [32].**

For test pressures exceeding 5 MPa, the burning rate measurements appear to agree with what was seen by Katsumi et al., although there are too few overlapping points in this region to conclusively state that the burning rates agree. The aqueous HAN solution used by Katsumi was also capable of ignition at pressures lower than 4 MPa via ignition wire. While the burning rate values do not agree perfectly with what is reported by Katsumi et al., there does appear to be a similar behavior in the burning rate versus pressure plot across all batches. An increase in burning rate with an increase in pressure is seen in all of the plots, which reaches some maximum burning rate where there

appears to be a slope break in the burning rate. After this point, the burning rates appear to slowly decrease with increasing pressure, with some scatter at pressures greater than 9.5 MPa.

Further comparisons were done by conducting burning rate experiments with the 82 wt. % aqueous HAN solutions provided by AFRL. It was found that the AFRL HAN also produced the inflection point in the pressure trace similar to what was seen in the Sigma Aldrich-prepared HAN. Therefore, it appears that this increase in pressure past the point of liquid propellant burning is a behavior typical of HAN, and not unique to the Sigma Aldrich-prepared HAN. Before comparing the AFRL HAN against the Sigma Aldrich HAN, the burning rates between the inflection point method and the high-speed video were compared for the AFRL HAN and are shown in Figure 20.

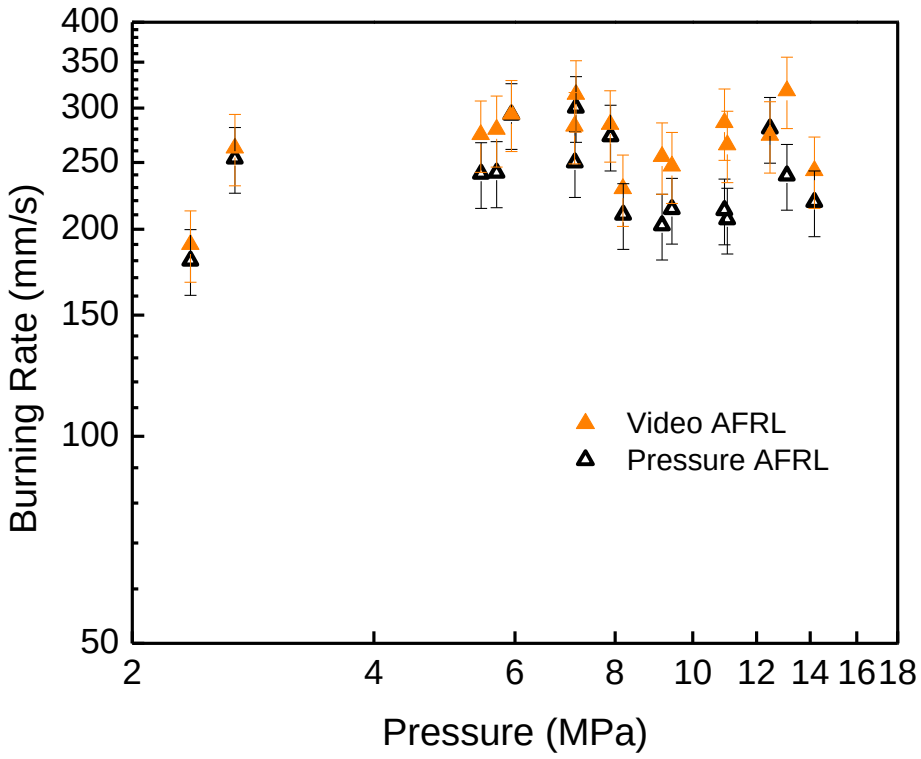


**Figure 20 - High-speed video versus inflection point burning rate measurements for 82 wt. % AFRL HAN.**

Similar to what was seen in the Sigma Aldrich-prepared HAN, it appears that either method for measuring the burning rate of the AFRL HAN may be used. However, there does appear to be significantly more scatter between the two methods at test pressures between 9 MPa and 11 MPa, as well as for the 13.1-MPa pressures, where the high-speed video reported burning rates up to 50 mm/s faster. The AFRL HAN was also able to ignite at pressures below 4 MPa, which indicates there may be some composition difference between the two different sources of HAN. Additional burning rate measurements were done using the inflection point method, which were then compared

against the Sigma Aldrich-prepared HAN as well as against the data from Katsumi et al., and are seen in Figure 21.

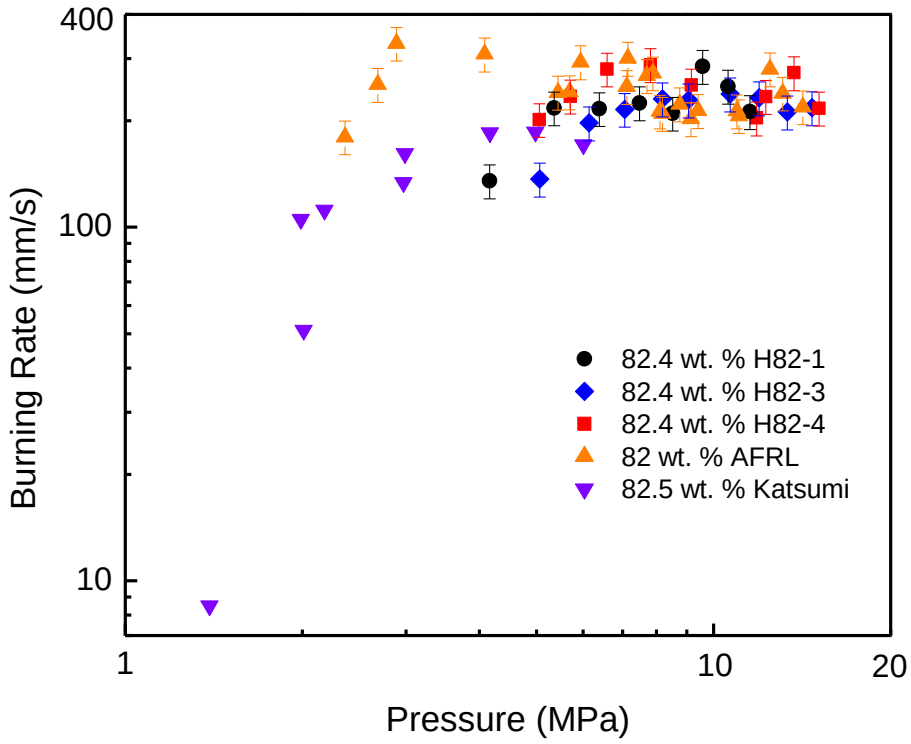


**Figure 21 - Comparison of AFRL HAN, Sigma Aldrich HAN, and Katsumi et al. [32].**

At test pressures below 5 MPa, there appears to be no agreement in the burning rate measurements between either source of HAN and the Katsumi et al. data. While the AFRL HAN was capable of igniting at test pressures lower than 5 MPa, several attempts were made to ignite the propellant at the test pressures used by Katsumi et al.; however there was no success in igniting the AFRL HAN at pressures below 2.37 MPa. The burning rates of the AFRL HAN were considerably higher than what was measured by

Katsumi for the pressures between 2.37 MPa and 4.25 MPa. Similar to what was stated in the comparison between the Sigma Aldrich HAN and the Katsumi et al. data, the AFRL HAN follows a similar trend of increasing burning rate with an increase in test pressure until it reaches some maximum burning rate, whereupon its burning rate slowly decreases with increasing pressure past this point. At pressures greater than 5 MPa, there appears to be agreement in the burning rate measurements between the AFRL HAN and the Sigma Aldrich HAN. Figure 22 provides a closer look for these test pressures.

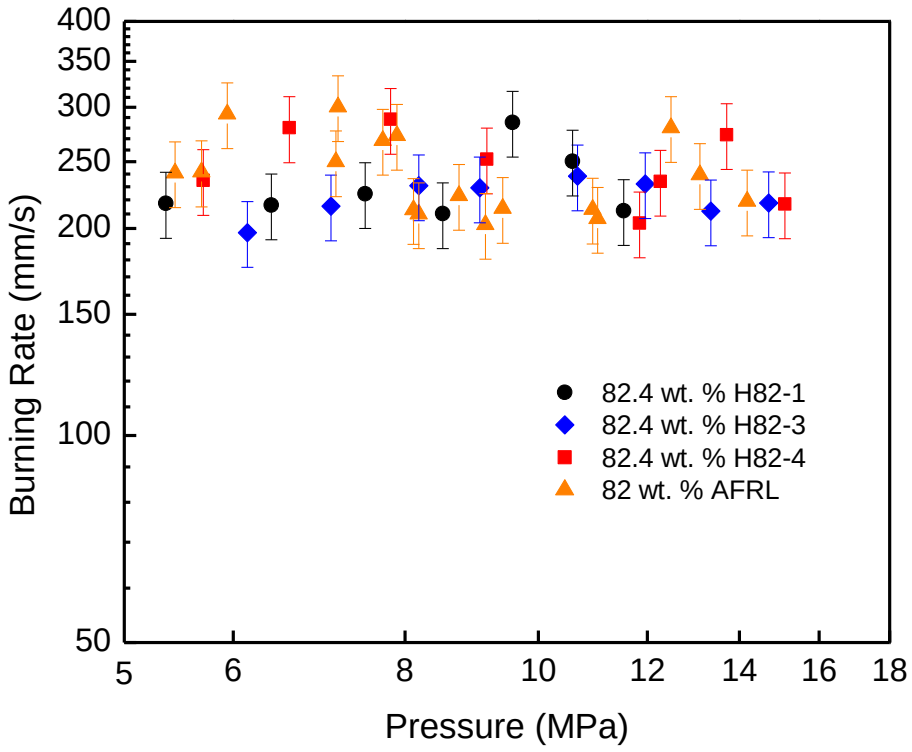


**Figure 22 - Comparison of inflection point burning rates at pressures greater than 5 MPa.**

In the test pressure range from 5 to 15 MPa, the burning rates measured across batches appear to agree with each other much better than at lower test pressures, although there appears to still be scatter between the batches. Some of the data scatter between the AFRL HAN and the Sigma Aldrich-supplied HAN may be attributed to the slight difference in wt. % concentration (0.4%) between the batches. However, the general, overall trend in burning behavior between the two sources of HAN appears to be the same.

### 4.3 Two-Phase HAN Combustion

Initial results indicate that either high-speed video or the inflection point method may be used to measure the burning rate of aqueous HAN. However, there remains the question of the unusual increase in pressure of the system once the liquid column of the aqueous HAN has completely burned. High-speed video images taken after the regression of the liquid phase show the presence of an opaque gas, as well as the formation of liquid droplets inside of the vessel. The presence of opaque gas as a result of aqueous HAN combustion has been reported by other researchers, and it is attributed to the formation of nitrogen dioxide due to its brown-red color [32], [40], [41]. Because the high-speed video camera used in these experiments is not capable of a colored image, it is assumed that the opaque gas seen in the video is the same as what is being reported by others. An example image of this gas can be seen in Figure 23, where the gas occupies the entire volume of the quartz tube as well as the environment outside of it. The time of this image falls within the timeframe of the pressure rise past the point of inflection, and the gas may be seen by the light produced from the nichrome wire.

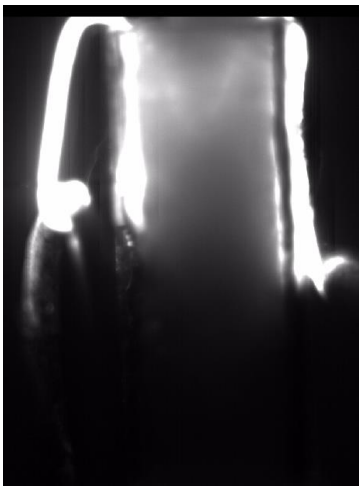

**Figure 23 - Presence of opaque gas inside of the quartz tube during the time of continued increase in pressure beyond the inflection point.**

This two-phase (liquid phase/gas phase) reaction of aqueous HAN has been reported before by Katsumi et al. [32] as detailed in the background literature. However, the gas phase has yet to be taken into account in any aqueous HAN burning rate measurements, as other groups utilized only visual-based methods. Additionally, no data reporting the pressure trace of aqueous HAN combustion could be found by the author at the time of this study. As such, this gas phase is only detailed as being the combustion products of the liquid-phase reaction. However, the increase in pressure past the point of the liquid phase of combustion is not insignificant, and at higher pressures produces an increase in pressure similar to the liquid phase of combustion. This rather large pressure rise appears to indicate that exothermic reactions are continuing to occur inside of the combustion environment after the liquid has completely combusted, and may be in the form of either gas-phase reactions of the combustion products or vaporization of residual liquid droplets. Figure 24 plots the pressure rise from the time of ignition to the

inflection point versus the pressure rise to the peak pressure for both the AFRL HAN and from Sigma Aldrich HAN batches.

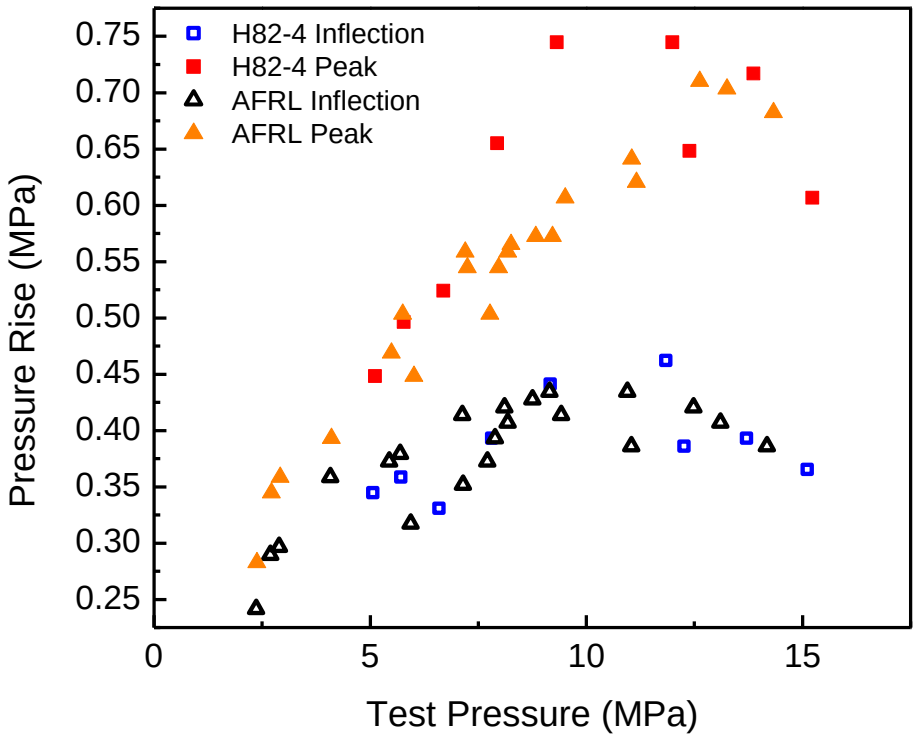


**Figure 24 - Pressure rise comparison between the inflection point and the peak pressure for both HAN sources.**

This figure shows how exothermic reactions are continuing to occur in the gas phase of the intermediate combustion species from the liquid phase which continues to increase the pressure inside of the constant-volume system. The pressure rise observed by the inflection point method increases with an increase in test pressure up to 10 MPa, where it decreases afterwards for both sources of HAN. It also appears that the gas-phase pressure rise increases by an even larger amount with an increase in test pressure,

as seen by the increasing gap between the inflection point pressure rise and the pressure rise for the peak pressure method for both sources of HAN. The Sigma Aldrich HAN follows the same trend for the peak pressure method with an increase in pressure rise with the increasing test pressure up to 10 MPa followed by a decrease in pressure rise for higher test pressures. However, the AFRL HAN pressure rise appears to continue to increase with an almost linear trend throughout the entire test pressure range.

It was decided to first determine whether this increase in pressure could potentially be due to the vaporization of the water inside of the solution from the heat of combustion. An approximation to determine the feasibility of this theory was done by treating the vaporization of water as an ideal gas at the adiabatic flame temperature of aqueous HAN combustion, then calculating the required mass in the vapor phase to produce the increase in pressure between the inflection point and the peak pressure. The adiabatic flame temperature of a mixture of 82.4 wt. % aqueous HAN was found by ProPEP 3 to be 839 K, and appears to be independent of test pressure after analyzing the flame temperature over the test pressure range (2 – 15.5 MPa). The results of the adiabatic flame temperature versus test pressure are shown in Appendix 5. Then, by using the gas constant of water vapor (462 J/kgK) with the known volume of the strand burner (0.00141 $m^3$), the mass of water required in grams to produce the change in pressure between the inflection point and the peak pressure was calculated, and the results are shown in Table 5 for ten aqueous HAN tests. This process is summarized by the modified ideal gas equation (5).

$$m_{H2O}(g) = \frac{\Delta P(MPa) * 0.00141 m^3}{462\ \frac{J}{kgK} * 839K} * 1000\ \frac{g}{kg} * 10^6\ \frac{Pa}{MPa} \quad (5)$$

**Table 5 - Mass of water required to be vaporized to produce the change in pressure between the inflection point and the peak pressure.**

| Trial | Test Pressure (MPa) | ΔP (MPa) | mass of water required (g) |
|---|---|---|---|
| 1 | 7.06 | 0.20 | 0.73 |
| 2 | 8.18 | 0.21 | 0.75 |
| 3 | 5.07 | 0.06 | 0.23 |
| 4 | 4.09 | 0.09 | 0.33 |
| 5 | 6.14 | 0.14 | 0.53 |
| 6 | 9.06 | 0.27 | 0.98 |
| 7 | 10.68 | 0.27 | 0.98 |
| 8 | 11.95 | 0.27 | 0.98 |
| 9 | 13.34 | 0.24 | 0.88 |
| 10 | 14.70 | 0.25 | 0.93 |

The typical total mass of aqueous HAN loaded into the strand burner for a test ranged from 0.9 to 1.1 g of propellant, so the required masses shown in Table 5 are

much too large for vaporization of water to be the cause of this increase in pressure of the system. This analysis indicates that gas-phase reactions are the likely contributor to the further increase in pressure after the liquid-phase burning.

It was decided to revisit the use of the peak-pressure method to measure the burning rate of aqueous HAN to capture its complete exothermic reaction. From this point on, the burning rates measured by use of the inflection point or high-speed video refer to the burning rates of the liquid phase of aqueous HAN combustion. The peak pressure method therefore is a method of measuring the burning rates of the two-phase combustion of aqueous HAN. Results for the two-phase burning rates of aqueous HAN are shown in Figure 25.

The burning rates for the two-phase aqueous HAN combustion are significantly lower than those measured in the liquid phase; however the general behavior in the plots is the same. Low burning rates are seen for the AFRL HAN at test pressures lower than 4 MPa. Afterwards, there is a peak burning rate achieved at test pressures between 4 and 5 MPa for all sources of HAN, followed by a decrease in burning rate afterwards up to 10 MPa, where there appears to be oscillations between an increase and decrease in the burning rate up to the 15 MPa test pressure. More interesting is that the two-phase burning rates for the AFRL HAN match more closely to those measured by Katsumi et al., even though Katsumi et al. utilized a visual burning rate method.

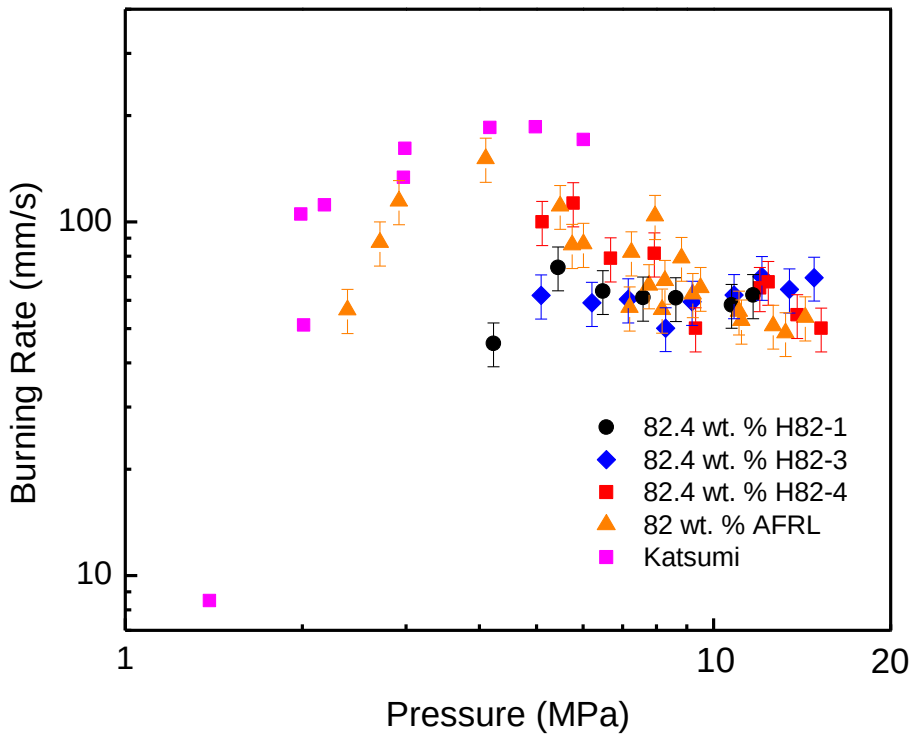


**Figure 25 - Two phase burning rate measurements via the peak pressure method.**

### 4.4 Detection of the Hydroxyl Radical

To determine whether the exothermic reactions occurring in the gas-phase burning region could be explained by combustion, an experiment to detect the excited-state hydroxyl radical, OH*, via chemiluminescence was done. The excited-state hydroxyl radical is very short lived, and it is a common species in combustion kinetics used to define the main flame region. The detection of OH* in the time frames of the gas-phase reaction would provide insight into whether combustion is occurring in this region.

To measure OH*, a Hamamatsu 1P21 photomultiplier tube was used with a 307-nm notch filter located at one of the sapphire optical windows. The photomultiplier tube was chosen over the photodetector because it provides a more-sensitive detector which would prove to be the more reliable method of measuring the smallest amounts of OH*. The 307-nm filter prevents any background light from overpowering the 307-nm emission of OH*. A high-voltage power supply was used to provide the source of excitation for the photomultiplier tube, and a resistor in parallel was used to prevent any overvoltage of the output signal from damaging the data acquisition electronics. The voltage output of the photomultiplier tube was recorded by the GageScope card. To verify whether the photomultiplier setup was functioning properly, a trial was conducted using nitromethane ignited via a solid propellant booster, which are both known to produce OH*. Figure 26 shows the pressure trace and output voltage of the photomultiplier tube for the solid propellant booster-ignited nitromethane test. The voltage of the power supply was set to 0.7 kV, and a 5.6 kΩ resistor was used.

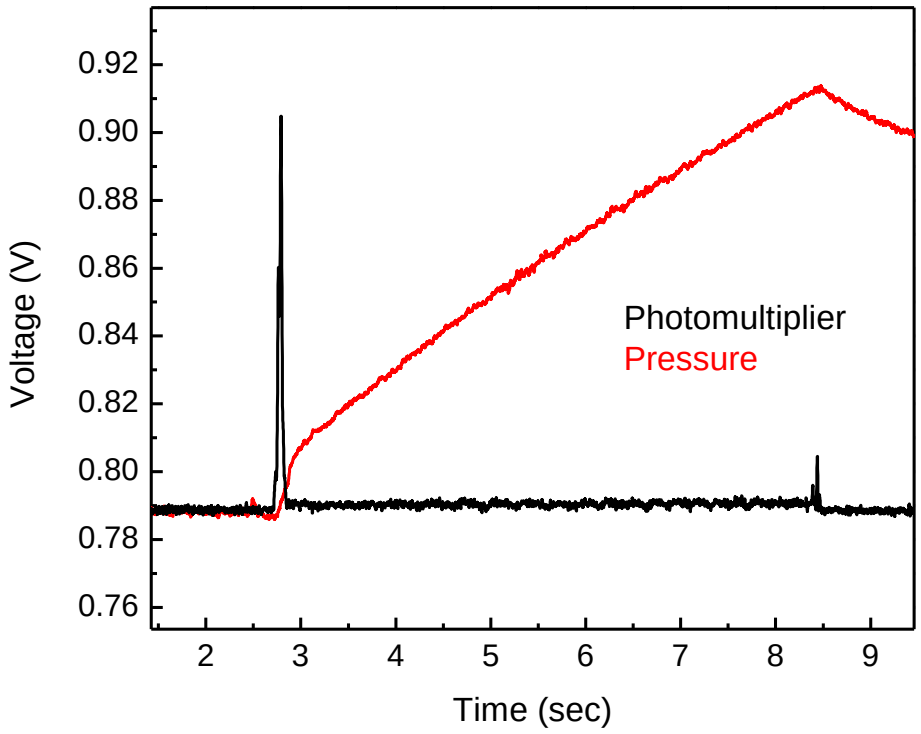


**Figure 26 - OH* produced by combustion of nitromethane at 8.6 MPa with a solid propellant booster ignition.**

There is a large signal voltage for the photomultiplier tube at the moment of ignition at 2.8 s, which indicates detection of OH* produced by the solid propellant booster. There is also a smaller signal voltage for the photomultiplier tube at the moment of burnout at 8.4 s, which may correspond to a change from a steady burn to incomplete combustion with the residual propellant. For the steady burning of nitromethane from 2.8 to 8.4 s, there is also the presence of the OH* radical, which can be seen in a closer look of the photomultiplier voltage output in Figure 27.

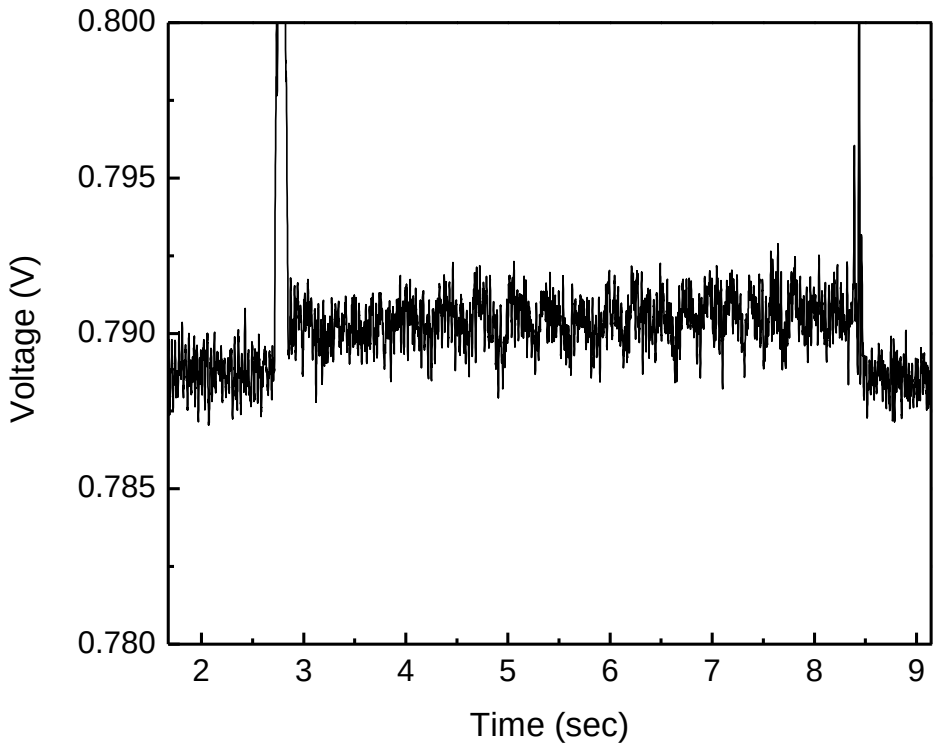


**Figure 27 - OH* produced by steady nitromethane burning.**

From this nitromethane test, it appears that the setup is capable of measuring OH* produced by nitromethane. Several voltage settings for the high-voltage power supply and resistors were used in an attempt to measure OH* produced by aqueous HAN, which are shown in Table 6. However, for all of these configurations, no discernable voltage output indicating the detection of OH* was found for either the liquid phase or gaseous phase. An example of the typical output is seen in Figure 28, which are the results for the 1-kV power supply voltage and 5.6-kΩ resistor.

**Table 6 - Various configurations of OH* detection for aqueous HAN.**

| Trial | Voltage (kV) | Resistor (kΩ) |
|---|---|---|
| 1 | 1 | 5.6 |
| 2 | 1 | 1 |
| 3 | 0.15 | N/A |

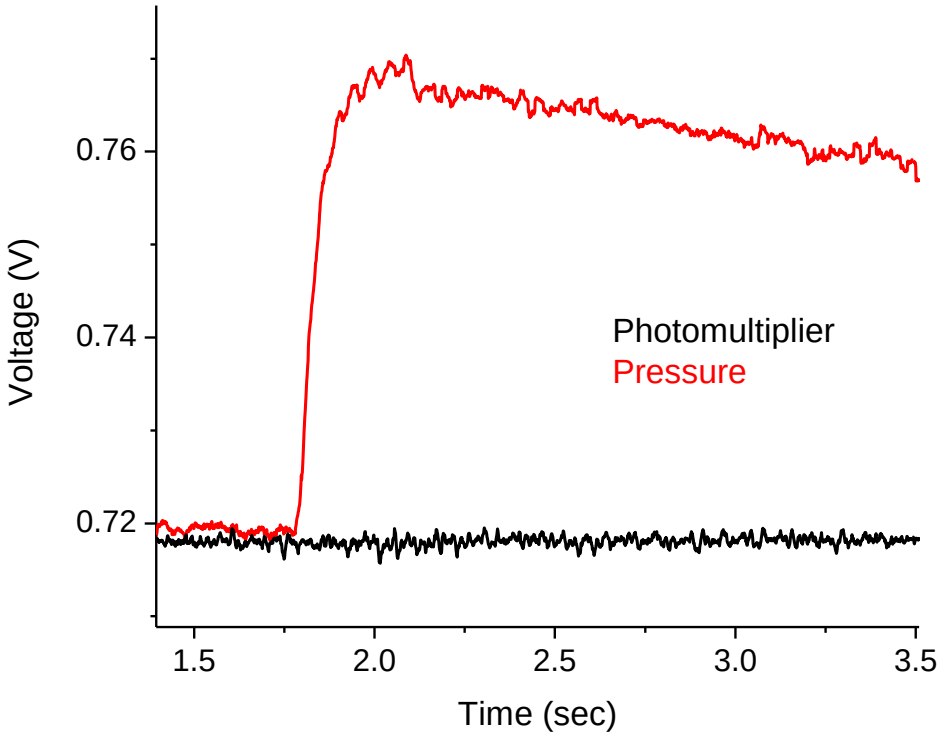


**Figure 28 - Voltage output of photomultiplier versus pressure trace for aqueous HAN at 7.38 MPa.**

These null results indicate that aqueous HAN produces little to no OH* in its combustion kinetics. Further investigations into determining gas-phase kinetic reactions may look for alternative intermediate reaction species in this region.

# 5. CONCLUSION

## 5.1 Present Study

The work of this thesis has shown that a method of measuring the burning rate of neat nitromethane and the liquid-phase burning rate of aqueous HAN via high-speed video has been developed and validated. These results also produced a second burning rate measurement for aqueous HAN which was defined to capture the two-phase burning behavior of aqueous HAN.

Neat nitromethane was tested at pressures ranging from 5.53 MPa to 13.06 MPa, where the burning rate measurements produced by both the peak-pressure method and by high-speed video agreed with results presented by others. Initial burning rate measurements of aqueous HAN by the peak-pressure method and the high-speed video at test pressures ranging from 4.13 MPa to 8.30 MPa resulted in drastically different burning rate values. It was found that the time where an inflection in the pressure trace of aqueous HAN is observed corresponded to the burnout time seen in the high-speed video. Adjusting the technique used to measure the burning rate of aqueous HAN by use of the inflection point of the pressure trace rather than the peak pressure resulted in burning rate values which agreed with those produced by high-speed video. Due to the continued increase in pressure for the strand burner system after this point in time, the burning rates measured by the inflection point and high-speed video were defined to be the burning rates for the liquid phase of aqueous HAN combustion.

The burning rates for two sources of aqueous HAN were compared against each other, resulting in similar burning rates at test pressures greater than 5 MPa. However,

the AFRL-sourced HAN was capable of igniting at test pressures much lower than what could be done with the Sigma Aldrich-sourced HAN, perhaps indicating some difference in the exact composition of the solutions. Furthermore, neither source of HAN resulted in burning rates which agreed with the burning rate measurements of aqueous HAN by Katsumi et al. [32]. This discrepancy indicates there may be some unresolved error in the chemical composition of aqueous HAN as a result of its production process.

The two-phase combustion behavior of aqueous HAN appears to contribute significant exothermic reactions, as seen by the continued increase in pressure of the system past the point of observed completion of the liquid-phase reaction. It was determined that vaporization of the water present in the aqueous solution is not feasible to be the sole cause of this continued pressure rise, indicating gas-phase kinetics of the combustion products. To fully capture the combustion behavior of aqueous HAN, the peak-pressure method originally used to measure the burning rates of propellants was used again to measure the two-phase burning rates of aqueous HAN. Efforts to measure the production of the A-X chemiluminescence of the hydroxyl radical for aqueous HAN provided no results for the presence of OH* throughout the liquid or gas-phase region.

## 5.2 Future Investigations

A study into the gas-phase reactions occurring from the aqueous HAN combustion products would further contribute to the understanding of the combustion characteristics of HAN. Laser diagnostic techniques have been used extensively to monitor for combustion products and combustion species as a means of developing chemical reaction processes for propellants. The use of these techniques for aqueous

HAN combustion could help determine the chemical kinetics present in the gas phase of the combustion products.

Investigations are currently underway at Texas A&M to determine the cause of different burning behaviors between the Sigma Aldrich and AFRL HAN at pressures lower than 5 MPa. One potential source of this difference may be the amount of free nitric acid present in the aqueous HAN solution, which is a known impurity as a result of HAN synthesis [42]. This difference may not only be as a result of HAN synthesis, but also as a result of the evaporation process used to increase the concentration of the Sigma Aldrich aqueous HAN. Nitric acid has a vapor pressure equal to 48 torr, which is much higher than the vapor pressure of water (17.56 torr). Therefore, some of this excess nitric acid may be removed as a result of this evaporation process. Initial titrations to measure this difference in acid have shown that the AFRL-supplied HAN is in fact more acidic than the Sigma Aldrich-supplied HAN. However, because HAN is itself acidic [42], this difference in acidity may also be caused by a variance in the concentration of HAN in the aqueous HAN solution. More thorough methods such as mass spectrometry or gas chromatography may provide more conclusive results to the exact concentrations of HAN, water, and nitric acid in a given propellant mixture.

# REFERENCES


[1] Edwards, T. "Liquid Fuels and Propellants for Aerospace Propulsion: 1903-2003," *Journal of Propulsion and Power,* Vol. 19, No. 6, 2003, pp. 1089-1107.

[2] Sutton, G.P., Biblarz, O., "Liquid Monopropellants", *Rocket Propulsion Elements*, 8th ed., John Wiley and Sons, Inc., Hoboken, NJ, 2010, p. 263.

[3] Mattingly, J.D., "Rocket Propulsion", *Elements of Propulsion: Gas Turbines and Rockets*, 1st ed., American Institute of Aeronautics and Astronautics, Reston, VA, 2006, p. 213.

[4] Jankovsky, R. S. "HAN-Based Monopropellant Assessment for Spacecraft," *American Institute of Aeronautics and Astronautics*, 1996, pp. 1-8.

[5] Sackheim, R.L, Buyers, D.C., "Status and Issues Related to In-Space Propulsion Systems," *Journal of Propulsion and Power*, Vol. 14, No. 5, 1998, pp. 669-675.

[6] Palaszewski, B., Ianovski, L.S., Carrick, P., "Propellant Technologies: Far-Reaching Benefits for Aeronautical and Space-Vehicle Propulsion," *Journal of Propulsion and Power,* Vol. 14, No. 5, 1998, pp. 641-648.

[7] Bobelli, V., Simon, D., Marée, T., Moerel, J.L., "Economic Benefits of the Use of Non-Toxic Mono-Propellants for Spacecraft Applications," in *39th AIAA/ASME/SAE/ASEE Joint Propulsion Conference and Exhibit*, Huntsville, AL, 2003.

[8] Schmidt, E.W., Wucherer, E.J., "Hydrazine(s) vs. Nontoxic Propellants - Where Do We Stand Now?," in *2nd Int. Conference on Green Propellants for Space Propulsion*, Cagliari, Sardinia, Italy, 2004.

[9] Spores, R.A., Masse, R., Kimbrel, S., McLean, C., "GPIM AF-M315E Propulsion System," in *49th AIAA/ASME/SAE/ASEE Joint Propulsion Conference & Exhibit*, San Jose, CA, 2013.

[10] Sackheim, R.L., Masse, R.K., "Green Propulsion Advancement: Challenging the Maturity of Monopropellant Hydrazine," *Journal of Propulsion and Power,* Vol. 30, No. 2, 2014, pp. 265-276.

[11] Gohardani, A.S., Stanojev, J., Demairé, A., Anflo, K., Persson, M., Wingborg, N., Nilsson, C., "Green space propulsion: Opportunities and prospects," *Progress in*

*Aerospace Sciences,* Vol. 71, 2014, pp. 128-149.

[12] Biddle, R.A., Sutton, E.S., "Highly soluble, non-hazardous hydroxylammonium salt solutions for use in hybrid rocket motors". United States of America Patent 4,527,389, 9 July 1985.

[13] Onodaka, S., Sakaue, K., Noguchi, R., Kuwahara, T., Yu, X., Shibamoto, H., "Ignition Characteristics of HAN Liquid for Gas-Hybrid Rockets," in *Joint Propulsion Conference*, San Jose, CA, 2013.

[14] Meinhardt, D., Brewster, G., Christofferson, S., Wucherer, E.J., "Development and Testing of New, HAN-Based Monopropellants in Small Rocket Thrusters," *American Institute of Aeronautics and Astronautics,* 1998, pp. 1-10.

[15] Klein, N., Coffee, T.P., Leveritt, C.S., "Pressure Oscillations in a Liquid Propellant Gun-Possible Dependence on Propellant Burning Rate," Ballistic Research Laboratory Aberdeen Proving Ground, Aberdeen, MD, 1992.

[16] Whitmore, S.A., Merkley, D.P., Eilers, S.D., Judson, M.I., Taylor, T.L., "Development and Testing of a Green Monopropellant Ignition System," in *49th AIAA/ASME/SAE/ASEE Joint Propulsion Conference and Exhibit*, San Jose, CA, 2013.

[17] Lee, H., Litzinger, T.A., "Chemical kinetic study of HAN decomposition," *Combustion and Flame,* Vol. 135, 2003, pp. 151-169.

[18] Wucherer, E.J., Christofferson, S.S., "Assessment of High Performance HAN-Monopropellants," *American Institute of Aeronautics and Astronautics,* 2000, pp. 1-10.

[19] Wu, M.H., Yetter, R.A., "A novel electrolytic ignition monopropellant microthruster based on low temperature co-fired ceramic tape technology," *Lab on a Chip,* Vol. 9, 2008, pp. 910-916.

[20] Klein, N., "Liquid Propellants for Use in Guns - A Review," US Army Ballistic Research Laboratory Aberdeen Proving Ground, Aberdeen, MD,1985.

[21] Decker, M.M., Klein, N., Freedman, E., Leveritt, C.S., Wojciechowki, J.Q., "HAN-Based Liquid Gun Propellants: Physical Properties," US Army Ballistic Research Laboratory Aberdeen Proving Ground, Aberdeen, MD, 1987.

[22] Oberle, W.F., Wren, G.P., "Burn Rates of LGP 1846 Conditioned Ambient, Hot, and Cold," U.S. Army Ballistic Research Laboratory Aberdeen Proving Ground,

Aberdeen, MD, 1991.

[23] McBratney, W.F., Vanderhoff, J.A., "High Pressure Windowed Chamber Burn Rate Determination of Liquid Propellant XM46," U.S. Army Research Laboratory Aberdeen Proving Ground, Aberdeen, MD, 1994.

[24] Chang, Y.P., Boyer, E., Kuo, K.K., "Combustion Behavior and Flame Structure of XM46 Liquid Propellant," *Journal of Propulsion and Power,* Vol. 17, No. 4, 2001, pp. 800-808.

[25] Vosen, S.R., "The Burning Rate of Hydroxylammonium Nitrate-Based Liquid Propellants," *Symposium (International) on Combustion,* Vol. 22, No. 1, 1988, pp. 1817-1825.

[26] Chang, Y.P., Kuo, K.K., "Assessment of Combustion Characteristics and Mechanism of a HAN-Based Liquid Monopropellant," in *37th AIAA/ASME/SAE/ASEE Joint Propulsion Conference and Exhibit,* Salt Lake City, UT, 2001.

[27] Masse, R.K., Overly, J.A., Allen, M.Y., Spores, R.A., "A New State-of-the-Art in AF-M315E Thruster Technologies," in *48th AIAA/ASME/SAE/ASEE Joint Propulsion Conference and Exhibit,* Atlanta, GA, 2012.

[28] Quach, P., Brand, W.A., "Adiabatic Compression Sensitivity of AF-M315E," in *51st AIAA/SAE/ASEE Joint Propulsion Conference*, Orlando, FL, 2015.

[29] Tsay, M., Lafko, D., Zwahlen, J., Costa, W., "Development of Busek 0.5N Green Monopropellant Thruster," in *27th Annual AIAA/USU Conference on Small Satellites*, Logan, UT, 2013.

[30] Vosen, S.R., "Concentration and Pressure Effects on the Decomposition Rate of Aqueous Hydroxylammonium Nitrate Solutions," *Combustion Science and Technology,* Vol. 68, 1989, pp. 85-99.

[31] Vosen, S.R., "Hydroxylammonium Nitrate-Based Liquid Propellant Combustion-Interpretation of Strand Burner Data and the Laminar Burning Velocity," *Combustion and Flame,* Vol. 82, 1990, pp. 376-388.

[32] Katsumi, T., Hori, K., Matsuda, R., Inoue, T., "Combustion Wave Structure of Hydroxylammonium Nitrate Aqueous Solutions," in *46th AIAA/ASME/SAE/ASEE Joint Propulsion Conference & Exhibit*, Nashville, TN, 2010.

[33] A. R. D. E. L. P. Kenneth W. McCown III, "Experimental Techniques to Study Linear Burning Rates of Heterogeneous Liquid Monopropellants," *Journal of Propulsion and Power,* vol. 30, no. 4, pp. 1027-1037, 2014.

[34] McCown, K.W., Demko, A.R., Petersen, E.L., "The Effects of Nano-Scale Additives on the Linear Burning Rate of Nitromethane at High Pressure," in *8th U.S. National Combustion Meeting*, Park City, UT, 2013.

[35] Warren, W., "Experimental Techniques for the Study of Liquid Monopropellant Combustion," Texas A&M University, College Station, TX, 2012.

[36] Sasse, R.A., Davies, M.A., Fifer, R.A., "Density of Hydroxylammonium Nitrate Solutions," U.S. Army Ballistic Research Lab Aberdeen Proving Ground, Aberdeen, MD, 1988.

[37] Homan-Cruz, G.D., "Experimental Techniques to Study the Combustion of Aqueous Solutions of Hydroxylammonium Nitrate with Additives," Texas A&M University, College Station, TX, 2015.

[38] Boyer, E., Kuo, K.K., "High-Pressure Combustion Behavior of Nitromethane," in *35th AIAA/ASME/SAE/ASEE Joint Propulsion Conference and Exhibit*, Los Angeles, CA, 1999.

[39] Sabourin, J.L, Yetter, R.A., Asay, B.W., Lloyd, J.M., Sanders, V.E., Risha, G.A., Son, S.F., "Effect of Nano-Aluminum and Fumed Silica Particles on Deflagration and Detonation of Nitromethane," *Propellants, Explosives, Pyrotechnics,* Vol. 34, 2009, pp. 385-393.

[40] Van Dijk, C.A., Priest, R.G., "Thermal Decomposition of Hydroxylammonium Nitrate at Kilobar Pressures," *Combustion and Flame,* Vol. 57, 1984, pp. 15-24.

[41] Kondrikov, B.N., Annikov, V.E., Egorshev, V.Y., De Luca, L.T., "Burning of Hydroxylammonium Nitrate," *Combustion, Explosion, and Shock Waves,* Vol. 22, No. 1, 2000, pp. 1817-1825.

[42] Decker, M.M., Freedman, E., Klein, N., Leveritt, C.S., Wojciechowski, J.Q., "Titrimetric Analysis of HAN-Based Liquid Propellants," Ballistic Research Laboratory Aberdeen Proving Ground, Aberdeen, MD, 1988.

APPENDICES

## Appendix 1 – Sample Holder Design 1

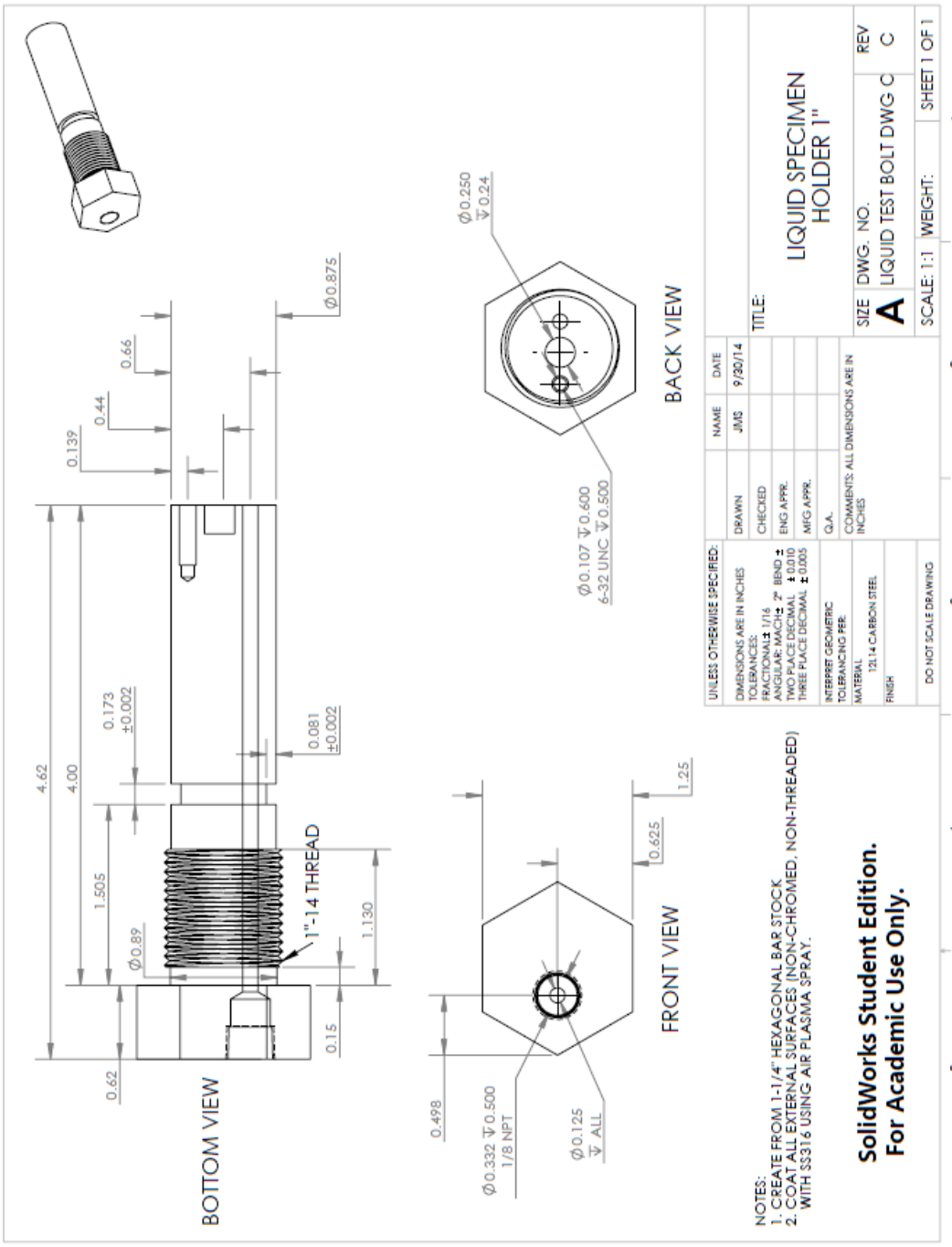

## Appendix 2 – Sample Holder Design 2

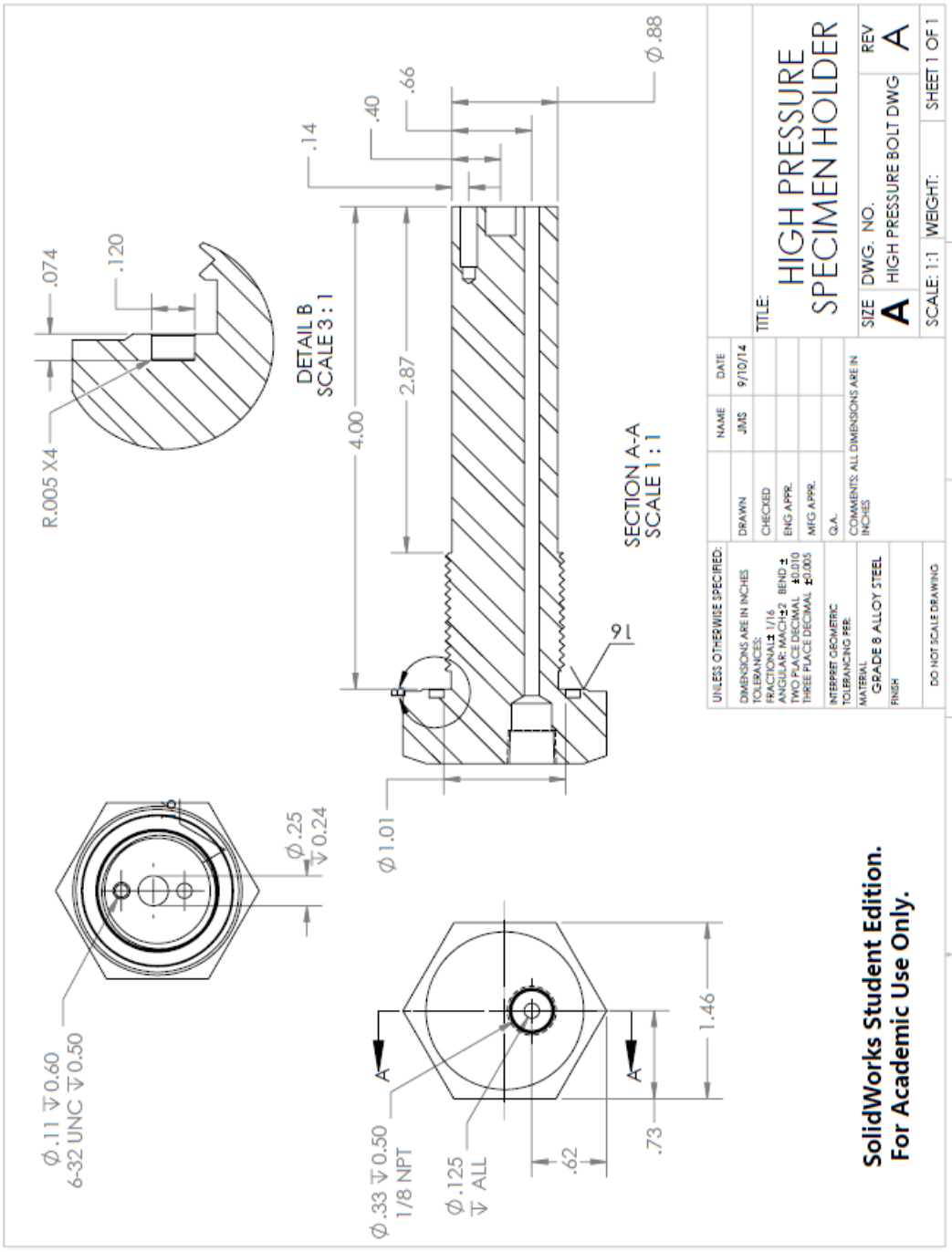

## Appendix 3 – Measurement Error Analysis

The measurement error analysis for the pressure based methods uses the assumptions of a constant density and constant diameter of the quartz tube to produce the following equation, A3.1. The weighted value of the measured mass burned $m_b$ is 0.02g because of the ±0.01g resolution scale used in the facility and a measured initial and final mass. The weighted value of the burn time is accurate to 0.01s, which is a conservative estimate of the ability to pinpoint the point of the slope changes defined as the times of ignition and burnout.

$$w_{rp} = \sqrt{\left(\frac{\partial r}{\partial m_b} * 0.02\right)^2 + \left(\frac{\partial r}{\partial \Delta t} * 0.01\right)^2} \tag{A3.1}$$

The simplification of r below with a constant density results in the following partial derivatives, which when used in A3.1 results in A3.2

$$r = \frac{m_b}{t_b}, \qquad \frac{\partial r}{\partial m_b} = \frac{1}{t_b}, \qquad \frac{\partial r}{\partial \Delta t} = \frac{-m_b}{{t_b}^2}$$

$$w_{rp} = \sqrt{\left(\frac{1}{t_b} * 0.02\right)^2 + \left(\frac{-m_b}{{t_b}^2} * 0.01\right)^2} \tag{A3.2}$$

The measurement error analysis for the high-speed video assumes a constant diameter of the quartz tube in its measurement process and results in equation A3.3. The weighted value of the measured column height, h is 0.02mm, a conservative estimate since we are able to select specific pixel locations quite accurately using PFV. The

resolution of the burn time is accurate to ±0.002s which is equivalent to the time between frames when using a framerate of 500 FPS, so a weight of 0.004s is used.

$$w_{rv} = \sqrt{\left(\frac{\partial r}{\partial h} * 0.02\right)^2 + \left(\frac{\partial r}{\partial \Delta t} * 0.004\right)^2} \tag{A3.3}$$

The equation for r is shown below with its respective partial derivatives.

$$r = \frac{h}{t_b}, \qquad \frac{\partial r}{\partial h} = \frac{1}{t_b}, \qquad \frac{\partial r}{\partial \Delta t} = \frac{-h}{{t_b}^2}$$

Which when used in A3.3 results in A3.4

$$w_{rv} = \sqrt{\left(\frac{1}{t_b} * 0.02\right)^2 + \left(\frac{-h}{{t_b}^2} * 0.004\right)^2} \tag{A3.2}$$

The tabulated errors for each test are shown in Table A3.1, where $r_i$ and $r_v$ are the burning rate measurements for the inflection method and video method, respectively. While $w_{r,i}$ and $w_{r,v}$ are the measurement errors.

**Table A3.1 - Measurement error for the inflection and high-speed video burning rates.**

| Test | Test Pressure (MPa) | $r_i$ (mm/s) | $r_v$ (mm/s) | $w_{r,i}$ (mm/s) | $w_{r,v}$ (mm/s) |
|---|---|---|---|---|---|
| H82-1-01 | 4.16 | 135.17 | 111.56 | 0.68 | 3.02 |
| H82-1-02 | 5.36 | 217.42 | 226.79 | 1.75 | 12.26 |
| H82-1-03 | 6.40 | 216.36 | 260.34 | 1.71 | 16.27 |
| H82-1-04 | 7.48 | 224.67 | 259.77 | 1.77 | 15.75 |
| H82-1-05 | 8.52 | 210.07 | 249.12 | 1.54 | 14.66 |
| H82-1-06 | 9.57 | 285.14 | 297.32 | 2.96 | 19.19 |
| H82-1-07 | 10.59 | 250.33 | 274.88 | 2.15 | 16.17 |
| H82-1-08 | 11.53 | 212.29 | 224.18 | 1.60 | 11.80 |
| H82-3-11 | 7.06 | 215.44 | 234.32 | 1.55 | 11.72 |
| H82-3-12 | 8.18 | 230.64 | 229.26 | 1.73 | 11.47 |

**Table A3.1 – Continued**

| Test | Test Pressure (MPa) | $r_i$ (mm/s) | $r_v$ (mm/s) | $w_{r,i}$ (mm/s) | $w_{r,v}$ (mm/s) |
|---|---|---|---|---|---|
| H82-3-13 | 5.07 | 136.73 | 130.32 | 0.62 | 3.73 |
| H82-3-15 | 6.14 | 197.14 | 198.72 | 1.28 | 8.64 |
| H82-3-16 | 9.06 | 229.01 | 226.30 | 1.77 | 11.32 |
| H82-3-18 | 10.68 | 238.23 | 249.51 | 1.89 | 13.49 |
| H82-3-19 | 11.95 | 232.16 | 228.91 | 1.78 | 11.17 |
| H82-3-20 | 13.34 | 211.88 | 235.98 | 1.56 | 12.42 |
| H82-3-21 | 14.70 | 217.79 | 208.87 | 1.57 | 9.50 |
| H82-4-01 | 11.84 | 203.66 | 226.04 | 1.42 | 16.05 |
| H82-4-02 | 9.17 | 252.28 | 255.93 | 1.97 | 18.83 |
| H82-4-03 | 7.81 | 288.08 | 270.33 | 2.56 | 20.46 |
| H82-4-04 | 6.59 | 280.05 | 258.72 | 2.61 | 20.56 |
| H82-4-05 | 5.71 | 234.77 | 212.90 | 1.74 | 14.28 |
| H82-4-06 | 5.06 | 201.57 | 194.29 | 1.34 | 13.19 |
| H82-4-07 | 12.26 | 234.19 | 236.96 | 1.96 | 19.68 |
| H82-4-08 | 13.71 | 273.54 | 239.31 | 2.70 | 19.23 |
| H82-4-09 | 15.11 | 217.09 | 228.01 | 1.86 | 19.34 |
| AFH82-5-02 | 5.44 | 240.78 | 274.68 | 2.09 | 17.72 |
| AFH82-5-03 | 5.94 | 293.45 | 294.25 | 3.13 | 21.02 |
| AFH82-5-04 | 7.89 | 272.98 | 284.10 | 2.63 | 18.33 |
| AFH82-5-05 | 5.69 | 241.56 | 279.38 | 1.94 | 16.44 |
| AFH82-5-06 | 8.18 | 209.96 | 229.13 | 1.46 | 11.46 |
| AFH82-5-07 | 9.42 | 213.83 | 247.29 | 1.57 | 12.68 |
| AFH82-5-08 | 11.04 | 206.65 | 265.35 | 1.61 | 15.17 |
| AFH82-5-09 | 7.15 | 300.44 | 314.32 | 3.18 | 20.28 |
| AFH82-5-10 | 12.48 | 280.23 | 273.87 | 2.69 | 17.67 |
| AFH82-5-11 | 14.18 | 219.03 | 243.32 | 1.77 | 13.91 |
| AFH82-5-12 | 13.10 | 239.47 | 318.08 | 2.09 | 23.56 |
| AFH82-5-13 | 9.15 | 202.67 | 255.30 | 1.49 | 15.48 |
| AFH82-5-14 | 10.95 | 213.27 | 285.97 | 1.61 | 18.45 |
| AFH82-5-15 | 7.12 | 249.97 | 282.61 | 2.12 | 18.24 |
| AFH82-5-16 | 8.11 | 212.94 | | 1.56 | |
| AFH82-5-17 | 7.71 | 268.39 | | 2.57 | |
| AFH82-5-18 | 8.75 | 223.17 | N/A | 1.75 | N/A |
| AFH82-5-19 | 4.08 | 308.86 | | 3.10 | |
| AFH82-5-20 | 2.89 | 331.41 | | 3.60 | |
| AFH82-5-21 | 2.69 | 253.33 | 262.54 | 2.13 | 15.45 |
| AFH82-5-22 | 2.36 | 180.06 | 190.08 | 1.11 | 8.64 |

As seen in Table A3.1, the errors for the burning rate measurements are relatively small, especially for the pressure based method. Therefore, this method was not applied to the peak pressure method, which used the statistical error method instead.

## Appendix 4 – Burning Rate Measurements for Aqueous HAN

### Table A4.1 - Burning rate measurements for liquid phase aqueous HAN and corresponding errors.

| Test | Test Pressure (MPa) | $r_i$ (mm/s) | $r_v$ (mm/s) | $error_i$ (mm/s) | $error_v$ (mm/s) |
|---|---|---|---|---|---|
| H82-1-01 | 4.16 | 14.82 | 111.56 | 14.82 | 13.25 |
| H82-1-02 | 5.36 | 23.83 | 226.79 | 23.83 | 26.94 |
| H82-1-03 | 6.40 | 23.72 | 260.34 | 23.72 | 30.92 |
| H82-1-04 | 7.48 | 24.63 | 259.77 | 24.63 | 30.86 |
| H82-1-05 | 8.52 | 23.03 | 249.12 | 23.03 | 29.59 |
| H82-1-06 | 9.57 | 31.26 | 297.32 | 31.26 | 35.32 |
| H82-1-07 | 10.59 | 27.44 | 274.88 | 27.44 | 32.65 |
| H82-1-08 | 11.53 | 23.27 | 224.18 | 23.27 | 26.63 |
| H82-3-11 | 7.06 | 215.44 | 234.32 | 23.62 | 27.83 |
| H82-3-12 | 8.18 | 230.64 | 229.26 | 25.28 | 27.23 |
| H82-3-13 | 5.07 | 136.73 | 130.32 | 14.99 | 15.48 |
| H82-3-15 | 6.14 | 197.14 | 198.72 | 21.61 | 23.60 |
| H82-3-16 | 9.06 | 229.01 | 226.30 | 25.11 | 26.88 |
| H82-3-18 | 10.68 | 238.23 | 249.51 | 26.12 | 29.64 |
| H82-3-19 | 11.95 | 232.16 | 228.91 | 25.45 | 27.19 |
| H82-3-20 | 13.34 | 211.88 | 235.98 | 23.23 | 28.03 |
| H82-3-21 | 14.70 | 217.79 | 208.87 | 23.87 | 24.81 |
| H82-4-01 | 11.84 | 203.66 | 226.04 | 22.33 | 26.85 |
| H82-4-02 | 9.17 | 252.28 | 255.93 | 27.66 | 30.40 |
| H82-4-03 | 7.81 | 288.08 | 270.33 | 31.58 | 32.11 |
| H82-4-04 | 6.59 | 280.05 | 258.72 | 30.70 | 30.73 |
| H82-4-05 | 5.71 | 234.77 | 212.90 | 25.74 | 25.29 |
| H82-4-06 | 5.06 | 201.57 | 194.29 | 22.10 | 23.08 |
| H82-4-07 | 12.26 | 234.19 | 236.96 | 25.67 | 28.15 |
| H82-4-08 | 13.71 | 273.54 | 239.31 | 29.99 | 28.42 |
| H82-4-09 | 15.11 | 217.09 | 228.01 | 23.80 | 27.08 |
| AFH82-5-02 | 5.44 | 240.78 | 274.68 | 26.39 | 32.63 |
| AFH82-5-03 | 5.94 | 293.45 | 294.25 | 32.17 | 34.95 |
| AFH82-5-04 | 7.89 | 272.98 | 284.10 | 29.93 | 33.75 |
| AFH82-5-05 | 5.69 | 241.56 | 279.38 | 26.48 | 33.19 |
| AFH82-5-06 | 8.18 | 209.96 | 229.13 | 23.02 | 27.22 |
| AFH82-5-07 | 9.42 | 213.83 | 247.29 | 23.44 | 29.37 |
| AFH82-5-08 | 11.04 | 206.65 | 265.35 | 22.65 | 31.52 |
| AFH82-5-09 | 7.15 | 300.44 | 314.32 | 32.94 | 37.33 |

**Table A4.1 - Continued**

| Test | Test Pressure (MPa) | $r_i$ (mm/s) | $r_v$ (mm/s) | $error_i$ (mm/s) | $error_v$ (mm/s) |
|---|---|---|---|---|---|
| AFH82-5-10 | 12.48 | 280.23 | 273.87 | 30.72 | 32.53 |
| AFH82-5-11 | 14.18 | 219.03 | 243.32 | 24.01 | 28.90 |
| AFH82-5-12 | 13.10 | 239.47 | 318.08 | 26.25 | 37.78 |
| AFH82-5-13 | 9.15 | 202.67 | 255.30 | 22.22 | 30.32 |
| AFH82-5-14 | 10.95 | 213.27 | 285.97 | 23.38 | 33.97 |
| AFH82-5-15 | 7.12 | 249.97 | 282.61 | 27.40 | 33.57 |
| AFH82-5-16 | 8.11 | 212.94 | | 23.34 | |
| AFH82-5-17 | 7.71 | 268.39 | | 29.42 | |
| AFH82-5-18 | 8.75 | 223.17 | N/A | 24.46 | N/A |
| AFH82-5-19 | 4.08 | 308.86 | | 33.86 | |
| AFH82-5-20 | 2.89 | 331.41 | | 36.33 | |
| AFH82-5-21 | 2.69 | 253.33 | 262.54 | 27.77 | 31.18 |
| AFH82-5-22 | 2.36 | 180.06 | 190.08 | 19.74 | 22.58 |

**Table A4.2 - Burning rate measurements for two-phase aqueous HAN and corresponding errors.**

| Test | Test Pressure (MPa) | $r_{pp}$ (mm/s) | $error_{pp}$ (mm/s) |
|---|---|---|---|
| H82-1-01 | 4.22 | 45.38 | 6.45 |
| H82-1-02 | 5.44 | 74.43 | 10.58 |
| H82-1-03 | 6.48 | 63.82 | 9.07 |
| H82-1-04 | 7.59 | 61.16 | 8.70 |
| H82-1-05 | 8.63 | 60.97 | 8.67 |
| H82-1-07 | 10.73 | 58.31 | 8.29 |
| H82-1-08 | 11.67 | 62.14 | 8.83 |
| H82-3-11 | 7.16 | 60.48 | 8.60 |
| H82-3-12 | 8.29 | 50.10 | 7.12 |
| H82-3-13 | 5.09 | 62.03 | 8.82 |
| H82-3-15 | 6.21 | 59.11 | 8.40 |
| H82-3-16 | 9.19 | 59.47 | 8.45 |
| H82-3-18 | 10.83 | 62.15 | 8.84 |
| H82-3-19 | 12.08 | 70.00 | 9.95 |
| H82-3-20 | 13.46 | 64.50 | 9.17 |
| H82-3-21 | 14.82 | 69.66 | 9.90 |
| H82-4-01 | 11.98 | 65.08 | 9.25 |
| H82-4-02 | 9.32 | 50.05 | 7.12 |
| H82-4-03 | 7.93 | 81.52 | 11.59 |

**Table A4.2 - Continued**

| Test | Test Pressure (MPa) | $r_{pp}$ (mm/s) | $error_{pp}$ (mm/s) |
|---|---|---|---|
| H82-4-04 | 6.68 | 78.98 | 11.23 |
| H82-4-05 | 5.77 | 113.03 | 16.07 |
| H82-4-06 | 5.11 | 100.07 | 14.23 |
| H82-4-07 | 12.39 | 67.76 | 9.63 |
| H82-4-08 | 13.87 | 54.60 | 7.76 |
| H82-4-09 | 15.23 | 50.04 | 7.11 |
| AFH82-5-02 | 5.48 | 111.10 | 15.80 |
| AFH82-5-03 | 6.01 | 86.76 | 12.33 |
| AFH82-5-04 | 7.96 | 104.10 | 14.80 |
| AFH82-5-05 | 5.75 | 86.16 | 12.25 |
| AFH82-5-06 | 8.26 | 68.25 | 9.70 |
| AFH82-5-07 | 9.51 | 65.19 | 9.27 |
| AFH82-5-08 | 11.16 | 52.65 | 7.49 |
| AFH82-5-09 | 7.25 | 82.10 | 11.67 |
| AFH82-5-10 | 12.62 | 50.91 | 7.24 |
| AFH82-5-11 | 14.33 | 53.75 | 7.64 |
| AFH82-5-12 | 13.25 | 48.55 | 6.90 |
| AFH82-5-13 | 9.22 | 62.58 | 8.90 |
| AFH82-5-14 | 11.05 | 55.87 | 7.94 |
| AFH82-5-15 | 7.20 | 57.33 | 8.15 |
| AFH82-5-16 | 8.18 | 56.54 | 8.04 |
| AFH82-5-17 | 7.77 | 66.32 | 9.43 |
| AFH82-5-18 | 8.82 | 79.20 | 11.26 |
| AFH82-5-19 | 4.10 | 151.10 | 21.48 |
| AFH82-5-20 | 2.92 | 114.60 | 16.29 |
| AFH82-5-21 | 2.71 | 87.60 | 12.45 |
| AFH82-5-22 | 2.38 | 56.41 | 8.02 |

It should be noted that there is a slight shift in test pressure between the liquid phase and two phase burning rates for the same tests. This shift is due to the process of calculating the test pressure by the average pressure for the test, which results in higher test pressure for the two phase burning rates due to its higher pressure at the point of burnout.

## Appendix 5 – Aqueous HAN Results from ProPEP 3

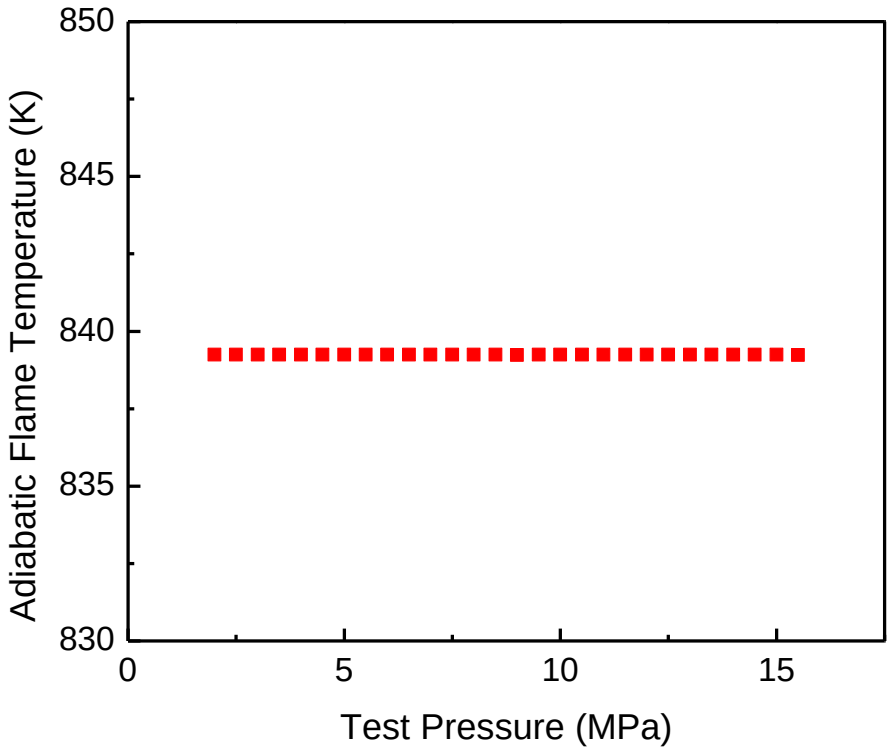


**Figure A5.1 - ProPEP 3 results for adiabatic flame temperature versus test pressure for 82.4 wt. % aqueous HAN.**

Figure A5.1 shows the adiabatic flame temperature for 82.4 wt. % aqueous HAN, which were found to be independent of the inputted chamber pressure. The initial temperature of the propellant was set to 298 K. The ProPEP 3 combustion products in mole fractions ($X$) for 1g of 82.4 wt. % aqueous HAN were $X_{H2O}$ = 0.611, $X_{N2}$ = 0.195, $X_{O2}$ = 0.195, $X_{NO}$ = 2.1E-06, and $X_{NO2}$ = 1.81E-06.